scientific reports

Check for updates

OPEN

Design and optimization of miniaturized co-planar Vivaldi antennas for enhanced microwave imaging in brain hemorrhage detection

Weijia Zhang[1,2,3,4,8], Jin Xie[1,8], Nutapong Somjit[1,2,3,5], Xue Cheng[1,2,3], Yanrong Jiang[1,2,3], Dongqin Sun[1,2,3], Xinghua Liu[1] & Shaomin Cai[2,3,6,7]✉

We designed and optimized a miniaturized coplanar Vivaldi antenna specifically for microwave imaging in cerebral hemorrhage detection. The antenna measures 80 mm × 80 mm × 1 mm and features an arc-shaped radiating arm, a 3 mm × 3 mm optimized pad layout, and an improved metallized via structure with nine vias, each 0.5 mm in diameter. These enhancements significantly improve the antenna's directivity, impedance matching, and signal penetration capability. Experimental results demonstrate that the antenna operates stably within the ultra-wide frequency band of 1.6–8 GHz, achieving a reflection coefficient as low as -45 dB at 4 GHz, a voltage standing wave ratio (VSWR) consistently below 1.5, and a peak gain of 9.5 dB at 6.5 GHz. These characteristics fully meet the sensitivity and penetration depth requirements for medical imaging. In addition to presenting a novel antenna design, this study validates its effectiveness under realistic biological conditions. Comparative analysis between 18- and 36-element antenna arrays demonstrates that the 36-element configuration improves image resolution and signal uniformity, while the 18-element array offers faster acquisition and better suitability for emergency or point-of-care screening scenarios. Additionally, in realistic skull model experiments, we employed rotating antenna technology (with a 20° step size) and multi-angle signal acquisition, further optimizing imaging uniformity and detection accuracy in hemorrhagic regions. By integrating real-time differential imaging technology and beamforming algorithms such as Delayed Sum (DAS) and Delayed Multiplication and Sum (DMAS), the experimental results indicate substantial progress in the identification of brain hemorrhage areas. This research provides critical technical support for the development of portable and non-invasive cerebral hemorrhage detection systems. Overall, by integrating miniaturization, performance optimization, and targeted enhancements, this study provides a robust technical basis for the development of early stroke detection systems.

Keywords Coplanar vivaldi antenna, Microwave imaging, Ultra-wideband (UWB), Brain hemorrhage detection

As the global population ages, the incidence and disability rates of brain diseases continue to rise. Statistics indicate that approximately 12.9 million new stroke cases occur worldwide each year, leading to about 5.4 million deaths[1]. Stroke has become a significant burden on global health, imposing considerable psychological and economic pressures on patients and their families, while also presenting a serious challenge to public health systems[4]. Given the current challenges in medicine, medical imaging technologies have advanced rapidly, with microwave imaging (MWI) emerging as a particularly promising approach. Compared to traditional imaging

[1]Department of Mathematica and Information Sciences, Shaoxing University, Shaoxing City, China. [2]Integrated Circuit Product Design Cooperation Base of Zhejiang, Shaoxing City, China. [3]Key Laboratory of Artificial Intelligence Multi-dimension Applications, Shaoxing University, Shaoxing City, China. [4]Department of AOP Physics, University of Oxford, Oxford, UK. [5]School of Electronic and Electrical Engineering, University of Leeds, Leeds, UK. [6]School of Medicine, Shaoxing University, Shaoxing City, China. [7]Shaoxing City Hospital, Shaoxing City, China. [8]These authors contributed equally: Weijia Zhang and Jin Xie. ✉email: usxmedlab@yeah.net

methods such as Computed Tomography (CT), MWI not only avoids radiation risks[2,3,5] but also offers high portability and low cost, making it especially suitable for early screening and long-term monitoring[6,7]. However, electromagnetic waves are significantly attenuated when penetrating biological tissues, which poses challenges to the resolution and deep tissue detection capabilities of existing microwave imaging systems. Therefore, selecting an appropriate antenna is crucial for ensuring imaging quality and diagnostic accuracy in MWI systems.

Currently, there are numerous types of antennas available for microwave imaging systems, including microstrip patch antennas[8,9] and monopole antennas[10]. While these antennas perform well in certain applications, their return loss and gain often do not meet high standards. In contrast, the Vivaldi antenna has demonstrated significant advantages in microwave imaging systems due to its superior performance. The Vivaldi antenna's UWB characteristics[11]allow it to cover a broad frequency range, achieve high gain, and maintain directional radiation. These properties effectively reduce external interference and improve imaging quality. As research progressed, researchers continuously optimized the Vivaldi antenna design using methods such as corrugated structures[12], dielectric loading[13], metamaterials[14], and improved feeding structures[15,16].These techniques further improved the antenna's radiation characteristics and increased its gain. For instance, Sivasankari et al.[17] proposed a Vivaldi antenna with a diamond-shaped slot, specifically tailored for biomedical applications. This antenna, constructed on a Flame Retardant 4 (FR4) substrate, measures 42.8 × 29.1 × 1.6 mm^3, operates in the frequency range of 3 GHz to 11 GHz, and achieves a gain of 5.8 dB. The diamond slot design effectively enhances the antenna's performance, particularly in wideband applications. Another example is the balanced slotted anti-dipole Vivaldi antenna proposed by Islam et al.[18], which measures 0.401λ × 0.401λ × 0.016λ. It operates in the frequency range of 3.01 GHz to 11 GHz, has a gain of 4.91 dB, and a return loss of approximately − 31 dB at 3.2 GHz. This antenna effectively detects breast tumors and shows promising application prospects.

Additionally, M. Y. I. Yazid et al.[19] developed a Sierpinski arrow curve slot Vivaldi antenna designed specifically for microwave head imaging. It uses a Rogers RO4350B substrate with a dielectric constant of 3.66, has dimensions of 65 × 65 × 1.6 mm^3, operates in the frequency band of 2.35 GHz to 3.79 GHz, and achieves a gain of 5.2 dB, with a return loss close to -35 dB at 3.5 GHz. This antenna effectively penetrates the head model, showing great potential for head imaging applications. Y. -h. Shi et al.[20] proposed a UWB high-gain Vivaldi antenna aimed at cerebral hemorrhage detection. It measures 0.29λ × 0.51λ × 0.005λ, operates in the frequency band of 0.8 GHz to 4 GHz, and achieves a gain of 7.05 dB, with a return loss near − 35 dB at 1.5 GHz. This design uses patch slotting and an added reflector to boost performance, especially at high frequencies. These enhancements allow more effective observation of brain electric field distributions and improve monitoring of signal changes during cerebral hemorrhage.

Parveen F et al.[21] utilized an antipodal Vivaldi antenna measuring 30.2 × 44.4 × 0.64 mm^3, with an operating frequency band of 2.75 GHz to 4.2 GHz, a maximum gain of 6 dB, and a return loss of less than − 8 dB. This antenna can locate abnormal areas, such as cerebral hemorrhage, by analyzing the peak intensity of different images, providing a preliminary location for lesions. Uyanik et al.[22] proposed a Modified Co-Planar Vivaldi Antenna (M-CPVA), sized at 58.6 × 92 × 1.6 mm^3, by modifying the exponential flare design of the traditional Vivaldi antenna. This design allows operation in the frequency band of 1 to 7.5 GHz, with a bandwidth of 15.2% and a return loss of -41 dB at 3.2 GHz. The antenna performed well in stroke monitoring, demonstrating excellent stability and accuracy through experimental validation. Lastly, Paul et al.[23] designed a compact UWB slot Vivaldi antenna with dimensions of 50 × 50 × 1.5 mm^3. This antenna achieves a return loss of -39 dB, a standing wave ratio of 1.001, and a peak gain exceeding 7 dB across the frequency range of 3.6 to 13.6 GHz, making it a strong contender in microwave imaging applications.

Although some antennas have demonstrated good performance in specific applications, many existing designs still fall short of meeting the requirements for high-precision imaging, particularly regarding return loss and gain. This is especially critical in deep tissue imaging, where signal attenuation can significantly diminish image clarity and, consequently, diagnostic accuracy. Furthermore, certain antennas fail to fully optimize impedance matching, leading to signal reflections and losses that reduce transmission efficiency. Additionally, the bandwidth of many existing antennas may not be sufficient to support efficient operation across multiple frequency bands. The miniaturization of antenna designs can also result in reduced gain, adversely affecting overall performance. Notably, the width of the microstrip line directly impacts its characteristic impedance[25–27]. Additionally, materials like FR4 substrates can incur significant dielectric and conductor losses at high frequencies, which further exacerbate signal attenuation issues.

To address these challenges, this paper presents a miniaturized coplanar Vivaldi antenna, building upon the traditional Vivaldi design. Enhancements include the introduction of a circular arc structure at the end of the radiating arm, along with optimizations in pad layout and metallized via design. The resulting antenna measures 80 mm × 80 mm × 1 mm, exhibits wideband characteristics in the 1.6 to 8 GHz frequency range, and demonstrates excellent reflection coefficient, standing wave ratio, and gain performance, thereby meeting the deep tissue detection requirements for microwave imaging systems in cerebral hemorrhage detection. To thoroughly validate the antenna's performance and practicality, this study combines simulation analysis with experimental testing using realistic skull models. We employed a multi-layer head model for in-depth testing to ensure the antenna's performance aligns with real biological conditions. The experimental results indicate that the antenna exhibits excellent imaging capabilities in complex tissue environments, confirming its effectiveness for early diagnosis of cerebral hemorrhage.

Design and simulation of a miniaturized co-planar Vivaldi antenna

In this study, we designed and optimized a miniaturized co-planar Vivaldi antenna specifically for detecting brain lesions. This antenna is widely utilized in high-resolution microwave imaging due to its broad bandwidth, high gain, and excellent directivity. To enhance the antenna's performance and stability, we incorporated a circular arc structure, optimized the pad design, and improved the configuration of the metallized vias. The circular

arc structure effectively reduces sidelobe radiation and enhances the antenna's directivity, while also improving energy radiation efficiency. The optimized pad design minimizes signal reflection and loss, further enhancing high-frequency bandwidth performance. Additionally, the metallized through-hole design facilitates improved signal penetration into deep brain tissue. Comprehensive validation was conducted across the frequency range of 1.6 GHz to 8 GHz using ANSYS simulation software.

Antenna configuration and parameterization study

The traditional Vivaldi antenna primarily consists of a dielectric substrate, a feeding system, and radiating arms. The dielectric substrate is made from polytetrafluoroethylene (PTFE), which has a relative permittivity of 2.65, a loss tangent of 0.0015, and a thickness of 0.762 mm. This material selection ensures excellent electromagnetic performance within the microwave frequency range. The dimensions of the Vivaldi antenna, specifically the length L and width W, can be calculated using the following expressions[28]:

$$L = \frac{\mathrm{C}}{\mathrm{f_1}}\sqrt{\frac{2}{\epsilon_{\mathrm{sub}}+1}} \tag{1}$$

$$W = \frac{\mathrm{C}}{2\mathrm{f_1}\sqrt{\epsilon_{\mathrm{sub}}}} \tag{2}$$

where C is the speed of light, $\mathrm{f_1}$ is the antenna's lowest frequency, and ϵ_{sub} is the dielectric constant of the substrate.

$$y = \pm\left(\mathrm{C_1 e^{rx}} + \mathrm{C_2}\right) \tag{3}$$

$$r = \frac{1}{\mathrm{L}} \cdot \ln\left(\frac{\mathrm{W}}{\mathrm{W_0}}\right) \tag{4}$$

$$\mathrm{C_1} = \frac{\mathrm{y_2}-\mathrm{y_1}}{\mathrm{e^{rx_2}}-\mathrm{e^{rx_1}}} \tag{5}$$

$$\mathrm{C_2} = \frac{\mathrm{y_2 e^{rx_2}}-\mathrm{y_1 e^{rx_2}}}{\mathrm{e^{rx_2}}-\mathrm{e^{rx_1}}} \tag{6}$$

where (x_1,y_1) and (x_2,y_2) represent the start and end coordinates of the tapered slot line, W_0 is the width of the rectangular transition slot, and r is the curvature of the tapered slot line, which determines the degree of curvature as defined in Eq. (4)[29]. According to Pérez M et al. the curvature r plays a crucial role in optimizing the antenna's gain and reflection coefficient, typically ranging from 0.25 to 0.45. When $r = 0$, the slot line becomes straight, leading to degraded bandwidth performance. Therefore, by adjusting the curvature factor r, the antenna's gain and directivity can be optimized to enhance electromagnetic performance[31]. In this design, we have chosen $r = 0.45$.

Quantitative analysis of circular arc sections at the end of the tapered slot line

In cerebral hemorrhage detection, it is essential for microwave signals to effectively penetrate brain tissues, particularly in deeper regions. This necessitates an antenna with strong energy concentration and significant penetration depth. To achieve this, we incorporated a circular arc section at the end of the gradient slot line, as illustrated in Fig. 1. This design minimizes secondary flap radiation and enhances the energy efficiency of the primary flap. Utilizing ANSYS simulation software, we analyzed the arc design with varying radii to optimize the antenna's performance, thereby improving both radiation strength and signal penetration.

Figure 2(a) presents the reflection coefficient results for antennas with different arc radii across the 1 GHz to 8 GHz frequency range. In the low-frequency range (1 GHz to 2 GHz), all antenna designs exhibit relatively high reflection coefficients, indicating poorer matching performance. Specifically, the design with a 0 mm radius

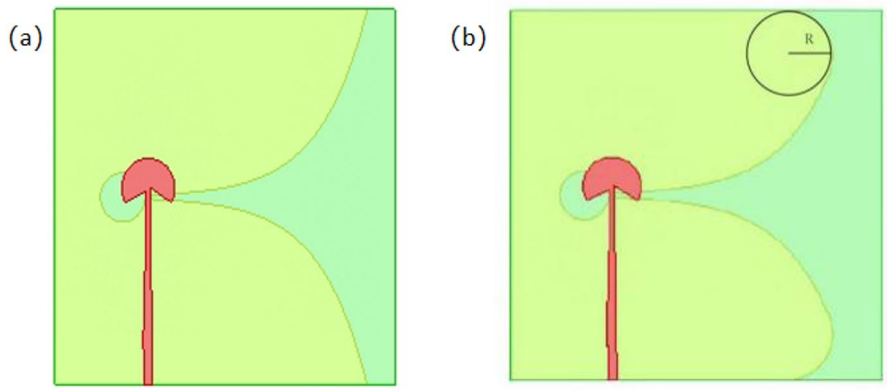

Fig. 1. Arc radius design in the Vivaldi antenna: (**a**) Traditional Vivaldi antenna; (**b**) Vivaldi antenna with an added circular arc at the end of the tapered slot line, with arc radius parameters of 5 mm, 7.5 mm, 10 mm, 12.5 mm, and 15 mm.

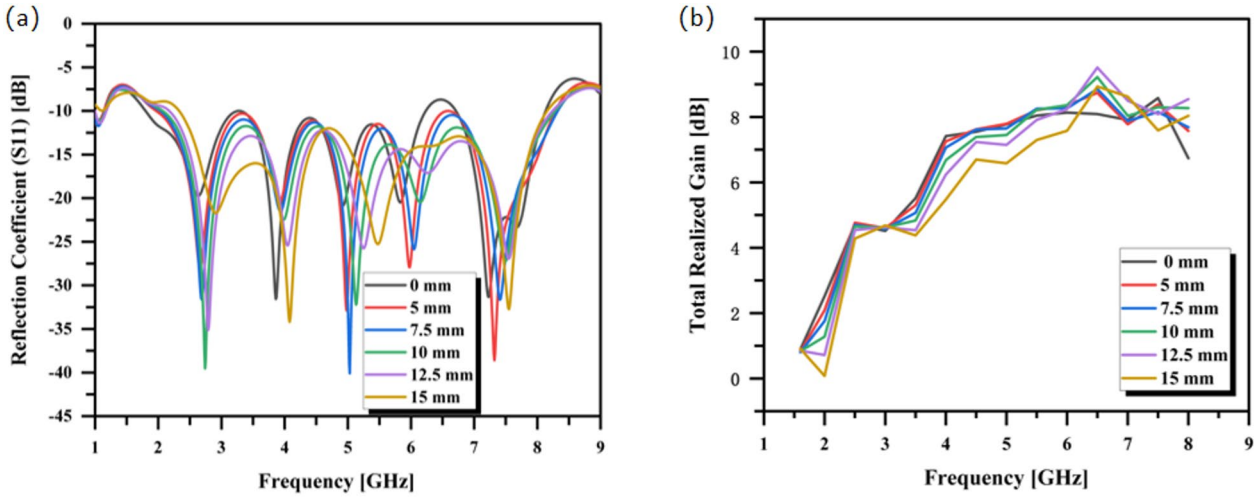

Fig. 2. Antenna performance with different arc radii (5 mm, 7.5 mm, 10 mm, 12.5 mm, and 15 mm): (**a**) Reflection Coefficient (S11); (**b**) Gain.

has a reflection coefficient of approximately − 10 dB, resulting in low transmission efficiency. The designs with 5 mm, 7.5 mm, and 10 mm radii show slight improvements, with reflection coefficients around − 12 dB, while the 12.5 mm and 15 mm designs demonstrate limited enhancement. In the mid-frequency range (2 GHz to 5 GHz), the 5 mm and 7.5 mm designs perform best at 5 GHz, achieving reflection coefficients close to -40 dB, while the 10 mm design reaches optimal performance around 3 GHz, with a reflection coefficient as low as -40 dB. In the high-frequency range (6 GHz to 9 GHz), all designs exhibit similar reflection coefficients, indicating stable matching performance. Overall, the 10 mm design performs optimally around 3 GHz and is well-suited for efficient signal transmission from 2 GHz to 3 GHz, making it particularly advantageous for medical imaging applications in the 1 GHz to 4 GHz range.

As shown in Fig. 2(b), the gain of all antenna designs in the 1.6 GHz to 8 GHz frequency range gradually increases with frequency. Notably, in the mid-frequency range (2 GHz to 4 GHz), the gain rises rapidly before stabilizing in the high-frequency range (5 GHz to 8 GHz). Although the 12.5 mm and 15 mm arc designs perform similarly to the 10 mm design in certain high-frequency bands (e.g., 7 GHz to 8 GHz), their gain curves display greater fluctuations, particularly a noticeable drop near 8 GHz, indicating less stability. The 5 mm and 7.5 mm arc designs show significant gain improvement in the 3 GHz to 5 GHz mid-frequency range but exhibit a downward trend at higher frequencies, limiting their applicability in high-frequency scenarios. In contrast, the 10 mm arc design performs exceptionally well across the entire frequency range, maintaining a smooth gain curve at a relatively high level. In the high-frequency range above 6 GHz, the gain remains stable at around 8 dB, peaking at approximately 9 dB at 6.5 GHz.

Figure 3 illustrates the radiation patterns of antennas with different arc radii at frequencies of 2.5 GHz, 4 GHz, 6 GHz, and 8 GHz. The smaller arc designs (0 mm, 5 mm, 7.5 mm) exhibit wider main lobes at lower frequencies (2.5 GHz), resulting in more scattered energy and weaker directivity, which is suitable for applications requiring broad coverage. However, as the frequency increases, sidelobe effects become more pronounced, affecting energy concentration in the high-frequency range. The larger arc designs (10 mm, 12.5 mm, 15 mm) demonstrate better directivity, particularly the 10 mm design, which excels in the 4 GHz to 6 GHz range. In this range, the main lobe is well-concentrated, sidelobe suppression is effective, and energy transmission efficiency is high, making it suitable for high-efficiency and high-directivity applications in the mid-frequency range.

In antenna design, the arc radius plays a crucial role in determining current distribution and energy transmission performance across various frequency bands, including 2 GHz, 4 GHz, 6 GHz, and 8 GHz. As illustrated in Fig. 4, smaller arc radii (such as 0 mm and 5 mm) demonstrate superior current distribution with lower losses in the lower frequency bands (2 GHz and 4 GHz). However, at higher frequencies (6 GHz and 8 GHz), there is a noticeable increase in current concentration, particularly at the curved sections of the antenna, where current density experiences a sharp rise. This phenomenon results in significant local radiation losses and diminished energy transmission efficiency. Conversely, larger arc radii (such as 10 mm and 12.5 mm) provide a more uniform current distribution across all frequency bands, especially at higher frequencies. The increased radius effectively reduces current concentration, thereby minimizing radiation losses associated with high local current density. Therefore, considering performance across different frequencies, an arc radius of 10–12.5 mm is optimal. This configuration not only enhances high-frequency performance but also maintains excellent energy transmission efficiency at lower frequencies, making it particularly suitable for multi-band antenna designs.

Pad design

In microwave signal transmission, pads play a crucial role in stabilizing signals, matching impedance, and optimizing signal quality. When the pad is integrated into the antenna structure with a curvature radius of 10 mm, adjusting the width of the pad can optimize the characteristic impedance Z_0 of the microstrip line, as shown

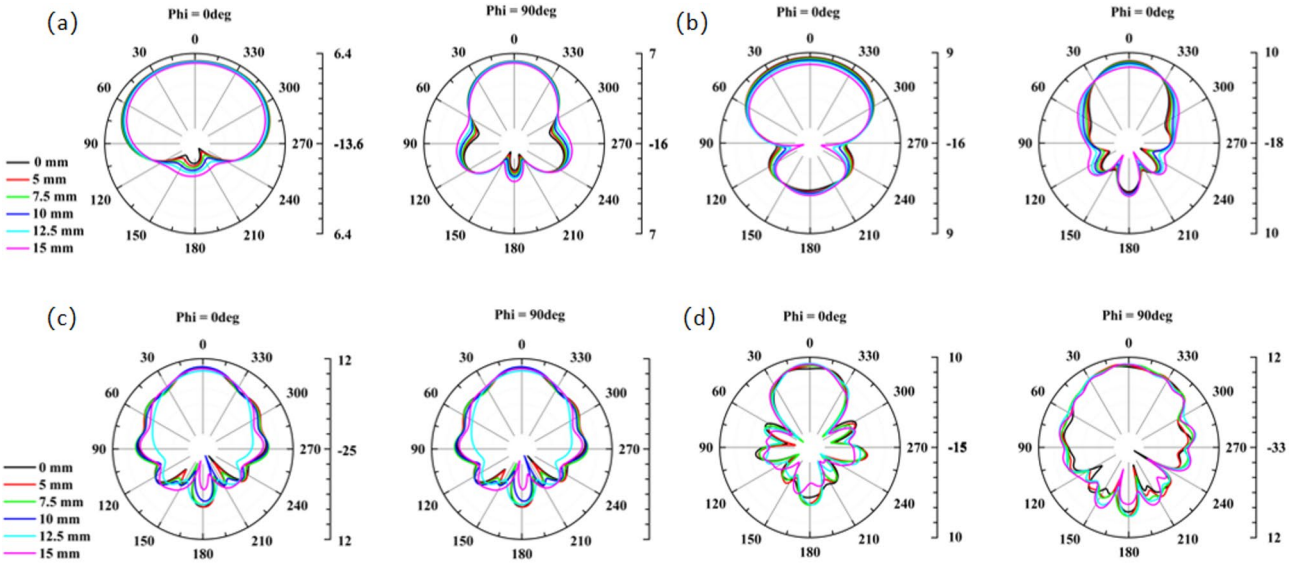

Fig. 3. Radiation patterns of antennas with different arc radius at different frequencies: (**a**) at 2.5 GHz; (**b**) at 4 GHz; (**c**) at 6 GHz; (**d**) at 8 GHz.

in Fig. 5(a), ensuring impedance matching with the feed line, minimizing signal reflection, and improving signal transmission efficiency. Specifically, the characteristic impedance Z_0 of the microstrip line is calculated using the following formula[30]:

$$Z_0 = \frac{60}{\sqrt{\epsilon_r}} \ln\left(\frac{4h}{W_{11}}\right) \tag{7}$$

where: Z_0 is the characteristic impedance of the microstrip line, ϵ_r is the relative permittivity of the substrate, h is the thickness of the substrate, W_{11} is the width of the pad.

We set the final pad dimensions to 3 mm × 3 mm to minimize reflections and losses during signal transmission. Although the simulation results (see Fig. 5(b)) indicate that variations in pad size have minimal impact on overall antenna performance, this optimization significantly enhances transmission stability at the signal input end and ensures effective impedance matching.

Metalized via design

In microwave imaging systems, ensuring the stability of signal transmission is critical. Metallized through-holes are employed to connect conductors between different layers of the antenna, facilitating efficient signal transmission within the multilayer structure. In this study, we integrate the metallized through-hole design into the optimized antenna structure, particularly in the two square pad regions, to further enhance the stability of the antenna's signal. The resistance R_{via} and inductance L_{via} of the vias directly impact the signal transmission and delay in the antenna, and their calculation formulas are as follows:

By increasing the number of vias N, a multi-path parallel conduction structure can be created, effectively improving the uniformity of current distribution. Based on the lumped parameter model, the total resistance function can be expressed as[30]:

$$R_{via} = \frac{\rho \cdot L_{via}}{A_{via}} = \frac{\rho \cdot l}{N \cdot \pi r^2} \tag{8}$$

where ρ is the metal resistivity, r is the via radius, L_{via} is the length of the via, A_{via} is the cross-sectional area of the via, and l is the effective conductive path length. Theoretical analysis shows that by increasing the number of vias N, the total resistance is significantly reduced, and Joule loss is minimized. Additionally, further optimization of via density based on skin depth can suppress surface eddy currents and optimize the electromagnetic field distribution.

The via diameter (D = 2r) influences impedance matching and thermal transfer efficiency by adjusting parasitic parameters. The expressions for parasitic inductance L_{via} and capacitance C_{via} are as follows[30]:

$$L_{via} = \frac{\mu \cdot L_{via}}{2\pi} \ln\left(\frac{2h}{r}\right) \tag{9}$$

$$C_{via} = \frac{\epsilon_r \epsilon_0 \pi r^2}{h} \tag{10}$$

$$Z_{via} = \sqrt{L_{via} \Big/ C_{via}} \tag{11}$$

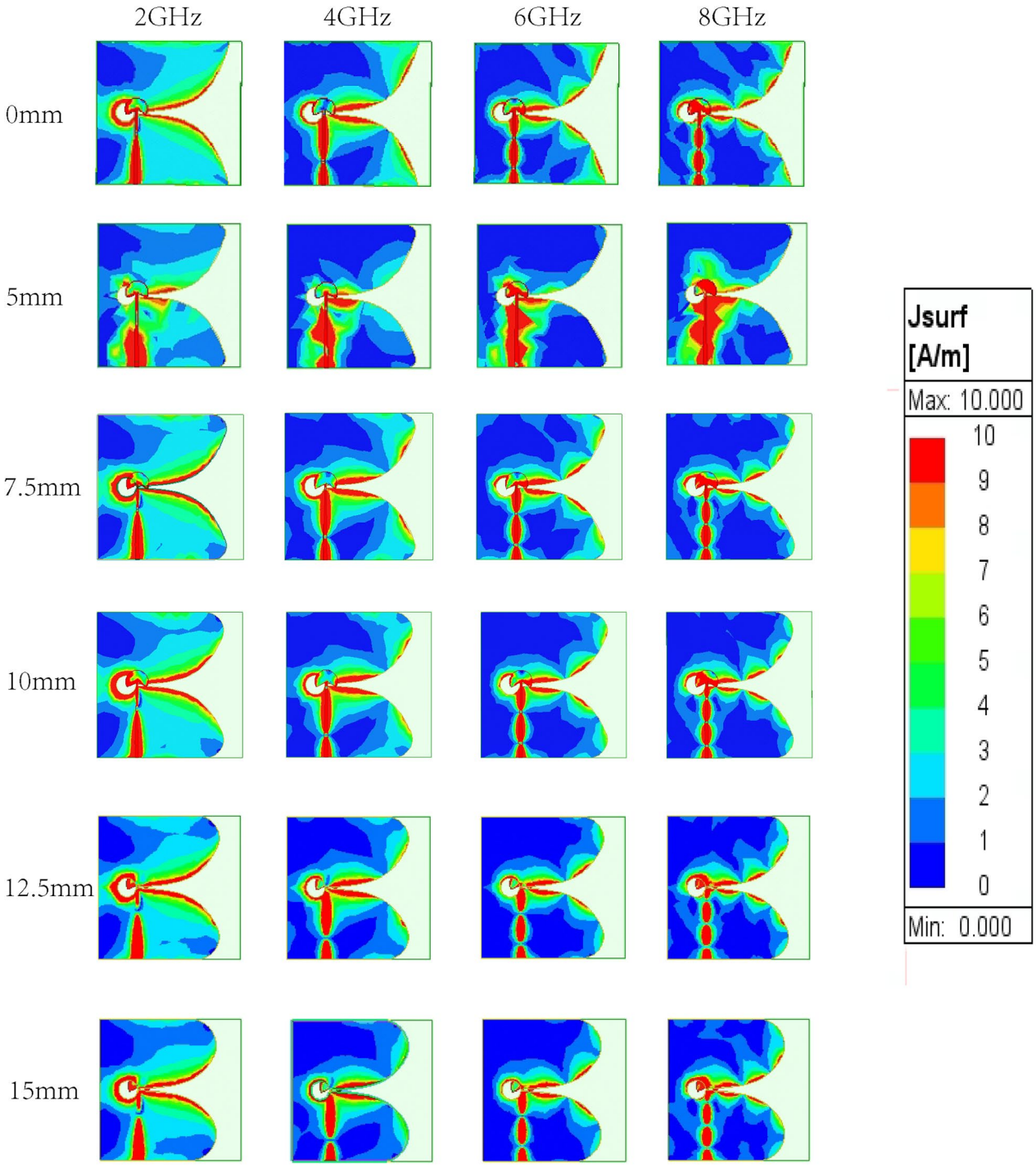

Fig. 4. Current distribution of antennas with different arc radii at various frequencies (2 GHz, 4 GHz, 6 GHz, 8 GHz).

The characteristic impedance Z_{via} must match the system impedance to reduce signal reflection. Increasing D can adjust the ratio of L_{via} and C_{via}, optimizing the wideband characteristics.

We conducted a detailed simulation analysis to understand how the number and diameter of vias affect the antenna's electrical performance. The analysis particularly focused on these parameters' impact on high-frequency signal transmission performance.

1) Adjustment and Analysis of Via Quantity.

The initial design included nine metallized vias. To explore the effect of via quantity on antenna performance, we adjusted the number of vias within the pad area, testing designs with 0, 2, 4, 6, and 9 vias, and analyzed their impact on the antenna's electrical properties.

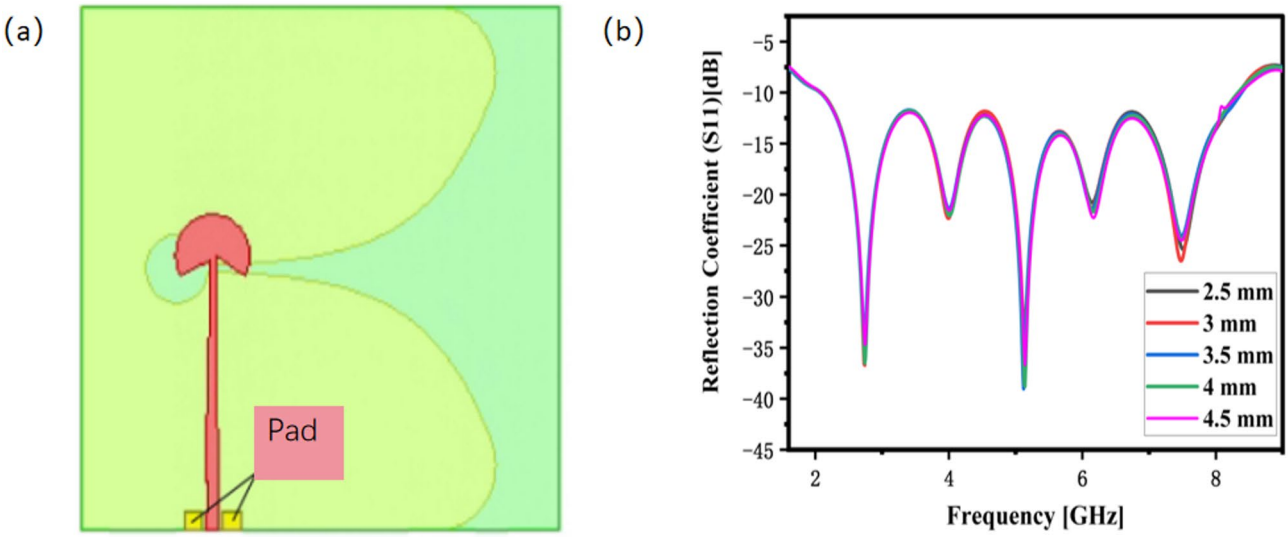

Fig. 5. Structural design and simulation results of the antenna with added pads: (**a**) Addition of pads to the antenna structure with a 10 mm arc radius; (**b**) Reflection coefficients (S11) for different pad side lengths, including 2.5 mm, 3 mm, 3.5 mm, 4 mm, and 4.5 mm.

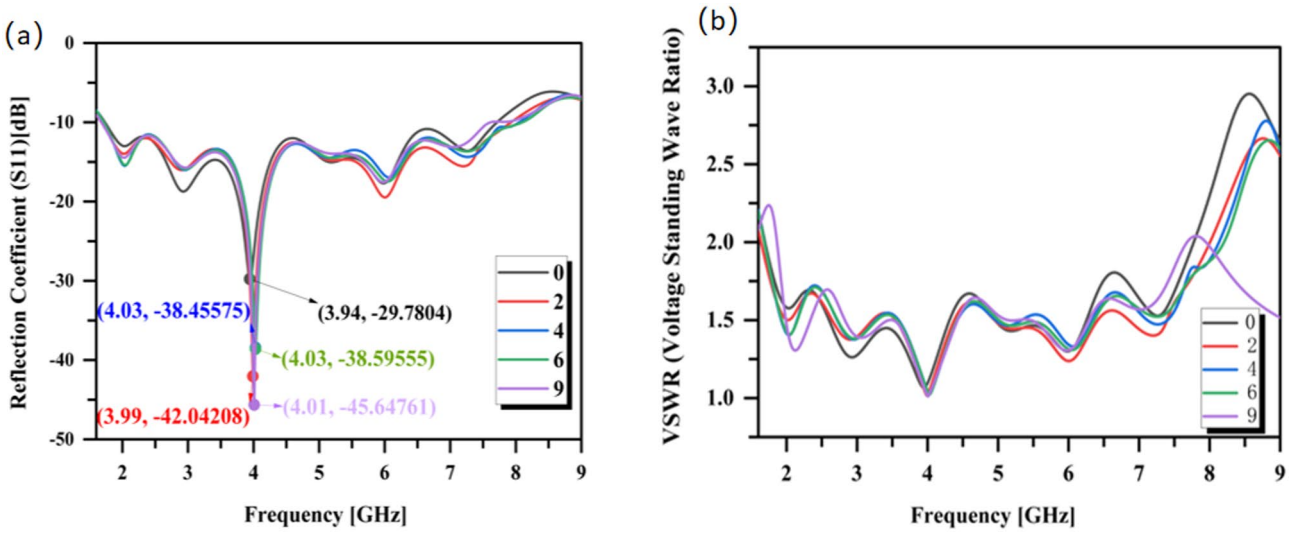

Fig. 6. Simulation results for different quantities of metalized vias (0, 2, 4, 6, and 9): (**a**) reflection coefficient; (**b**) VSWR.

Figure 6(a) displays the variation of the antenna's reflection coefficient (S11) with frequency for different quantities of vias. With nine vias, the antenna achieves a reflection coefficient of -45 dB at the 4 GHz band, indicating optimal impedance matching and minimal reflection loss. As the number of vias decreases, impedance matching worsens. For example, with two vias, the reflection coefficient remains around − 42 dB—close to the nine-via design—but shows slightly reduced stability in other frequency bands. With four and six vias, reflection coefficients drop to approximately − 38 dB, indicating poorer matching, likely due to parasitic effects from discontinuous electrical connections impacting signal transmission stability.

Figure 6(b) illustrates that in the low-frequency range (2 GHz to 4 GHz), the VSWR remains between 1 and 2.5, with the nine-via configuration yielding the lowest VSWR, indicating optimal impedance matching. In the mid-frequency range (4 GHz to 6 GHz), the VSWR fluctuates slightly between 1 and 1.5, demonstrating generally good matching across different via quantities. However, in the high-frequency range (6 GHz to 8 GHz), the VSWR gradually increases but remains below 2, indicating acceptable matching. In the ultra-high frequency range above 8 GHz, configurations with fewer than nine vias exhibit higher VSWR values, while the nine-via configuration shows a decrease, suggesting superior performance.

Figure 7 illustrates the variations in maximum gain and 3dB beamwidth in $\varphi = 0°$ and $\theta = 0°$ planes across different frequencies (1.5 GHz, 2.5 GHz, 4 GHz, 6 GHz, 8 GHz) and via quantities. Regardless of the plane, the

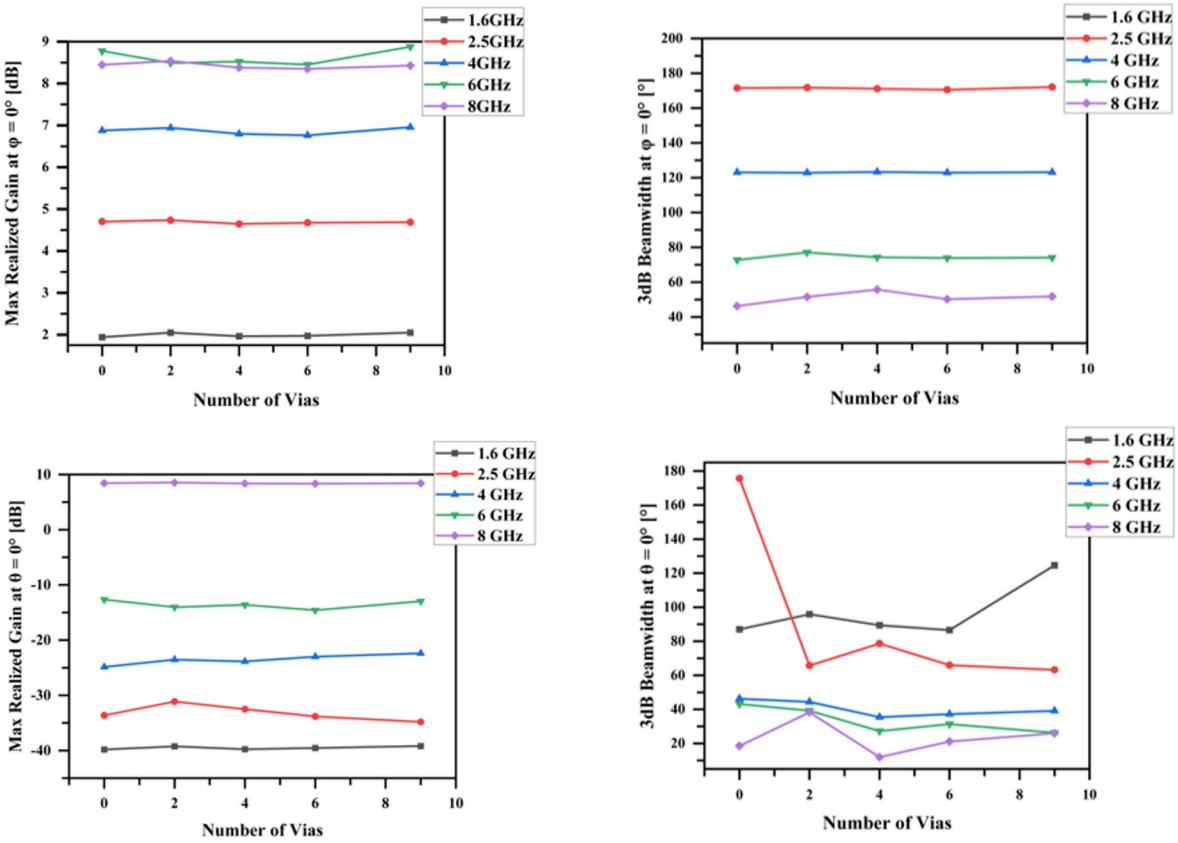

Fig. 7. Maximum Gain and 3dB Beamwidth at 1.5 GHz, 2.5 GHz, 4 GHz, 6 GHz, and 8 GHz for Antennas with Different Via Quantities in the φ = 0° and θ = 0° Planes.

maximum gain achieved by the antenna shows minimal change with varying via quantities, especially in high-frequency bands (6 GHz, 8 GHz), where the gain remains stable, indicating that via quantity has a negligible effect on high-frequency gain. In low-frequency bands (1.5 GHz and 2.5 GHz), there is a slight increase in gain, but the change is minimal. In high-frequency bands (6 GHz, 8 GHz), an increase in via quantity slightly enlarges the 3dB beamwidth, indicating a minor reduction in directivity and resulting in a broader beam. However, in low-frequency bands, changes in beamwidth are minimal.

2) Adjustment and Analysis of Via Hole Diameter.

To further optimize the antenna's electrical performance while keeping the number of vias constant, we varied the via hole diameter. A diameter that is too large may introduce parasitic inductive effects, while one that is too small could lead to poor electrical connectivity, thereby increasing reflection loss.

Figure 8(a) shows the variation in reflection coefficients at different frequencies for various via hole diameters. When the via diameter is 0.5 mm, the antenna achieves a reflection coefficient of -45 dB at 4 GHz, indicating optimal impedance matching. This design effectively reduces parasitic capacitance and inductance, ensuring minimal energy reflection and optimal signal transmission efficiency. In contrast, smaller diameters (e.g., 0.2 mm and 0.3 mm) lead to decreased matching performance due to enhanced parasitic effects. Larger diameters (e.g., 0.7 mm) still provide good matching but introduce more inductive effects, slightly increasing reflection loss. Therefore, a via diameter of 0.5 mm is recommended for antennas operating around 4 GHz to achieve optimal matching and minimal signal reflection.

Figure 8(b) illustrates the variations in VSWR with frequency for different via diameters. In the 1.6 GHz to 4 GHz range, the 0.5 mm via diameter demonstrates the lowest VSWR, indicating optimal matching performance. Between 4 GHz and 6 GHz, the VSWR remains stable, ranging from 1 to 1.75 across all diameters. However, in the 6 GHz to 8 GHz range, VSWR values increase, with the 0.5 mm diameter still providing the best performance by maintaining superior matching characteristics beyond 8 GHz.

Figure 9 illustrates the variations in maximum gain and 3dB beamwidth for different pore diameters at frequency bands of 1.6 GHz, 2.5 GHz, 4 GHz, 6 GHz, and 8 GHz. The 0.5 mm diameter exhibits the best performance at 4 GHz and 6 GHz, achieving gains of 7.5 dB and 8 dB, respectively, with beamwidth maintained between 70°and 75°, and minimal side lobe effects, ensuring a well-balanced trade-off between gain and beamwidth. Smaller diameters (0.2 mm and 0.3 mm) exhibit a wider beam at lower frequencies (1.6 GHz and 2.5 GHz), but at higher frequencies (6 GHz and 8 GHz), side lobe effects become more pronounced, leading to a gain reduction to 5 dB. Conversely, larger diameters (0.6 mm and 0.7 mm) achieve a gain increase up to 9 dB at 8 GHz, but with significant side lobe effects, negatively impacting radiation efficiency. In conclusion, the

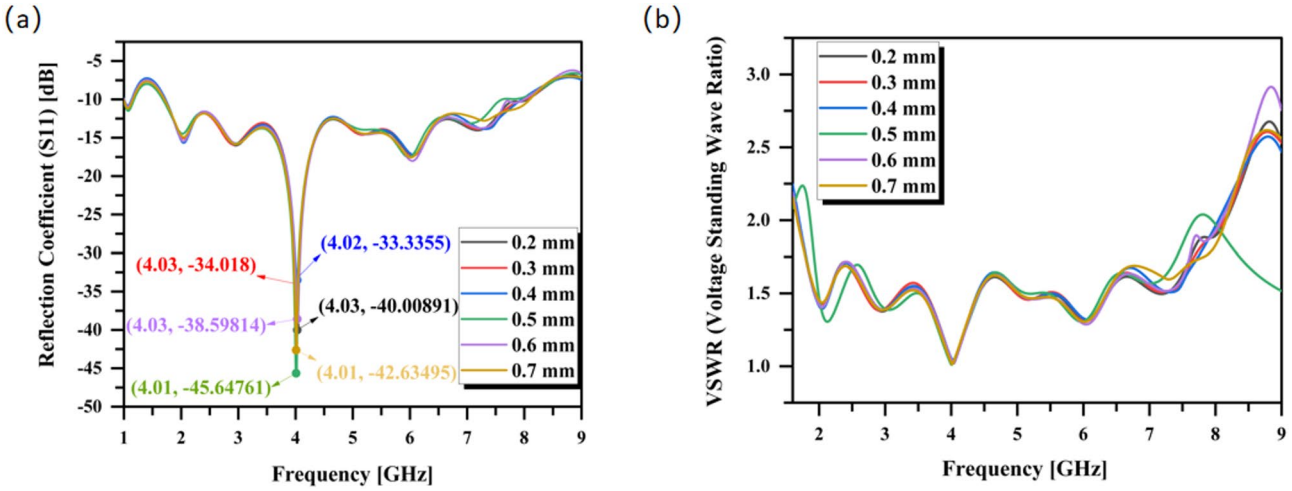

Fig. 8. Simulation results for different metal via hole diameters (0.2 mm, 0.3 mm, 0.4 mm, 0.5 mm, 0.6 mm, 0.7 mm): (**a**) Reflection coefficient; (**b**) VSWR.

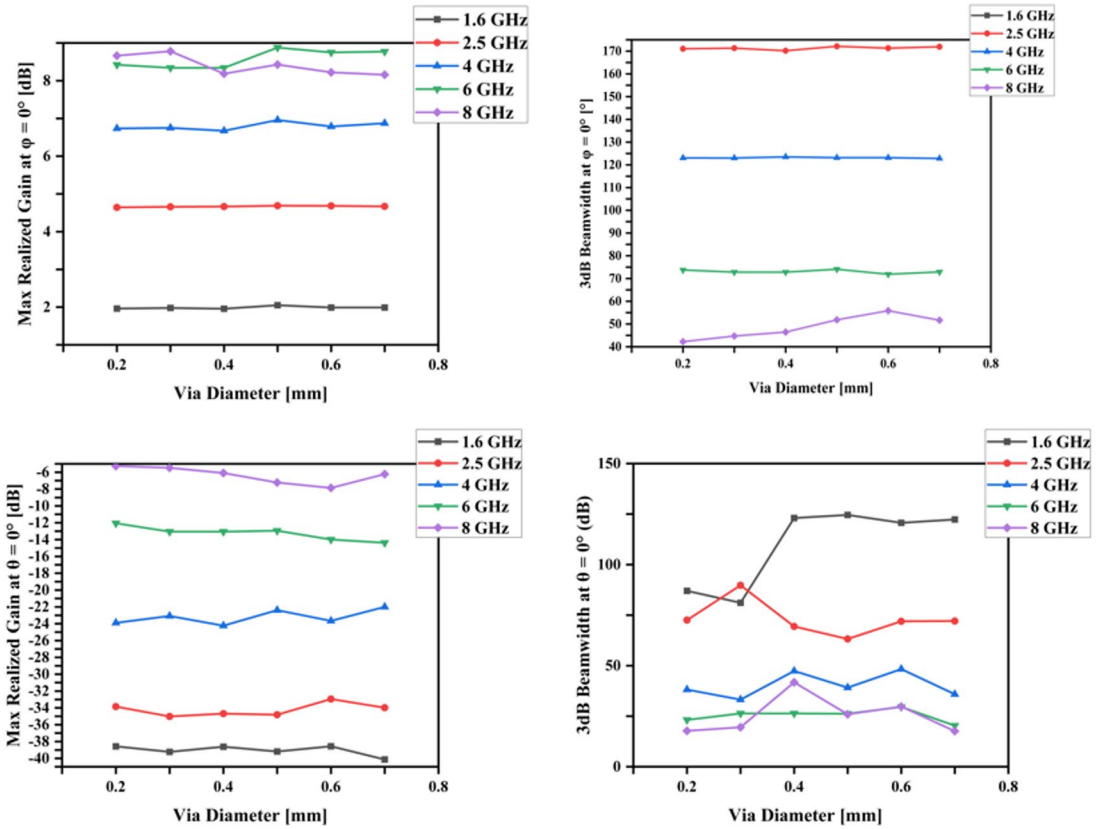

Fig. 9. Maximum gain and 3dB beamwidth of antennas with different via diameters at varying frequencies (1.5 GHz, 2.5 GHz, 4 GHz, 6 GHz, and 8 GHz) in $\varphi = 0°$ and $\theta = 0°$ planes.

0.5 mm diameter achieves the optimal balance between gain and directivity in the mid-to-high frequency range. Through optimized antenna design, the electromagnetic performance in the 1.6 GHz to 6 GHz frequency range has been significantly improved.

During the antenna design optimization, the optimal combination of a 10 mm arc radius, nine vias, and a 0.5 mm via diameter was determined through simulation analysis. The 10 mm arc radius exhibits optimal performance in the 2 GHz to 6 GHz range, greatly improving impedance matching, reducing side-lobe radiation, and enhancing directionality and energy transmission efficiency. The nine-via design further optimizes the

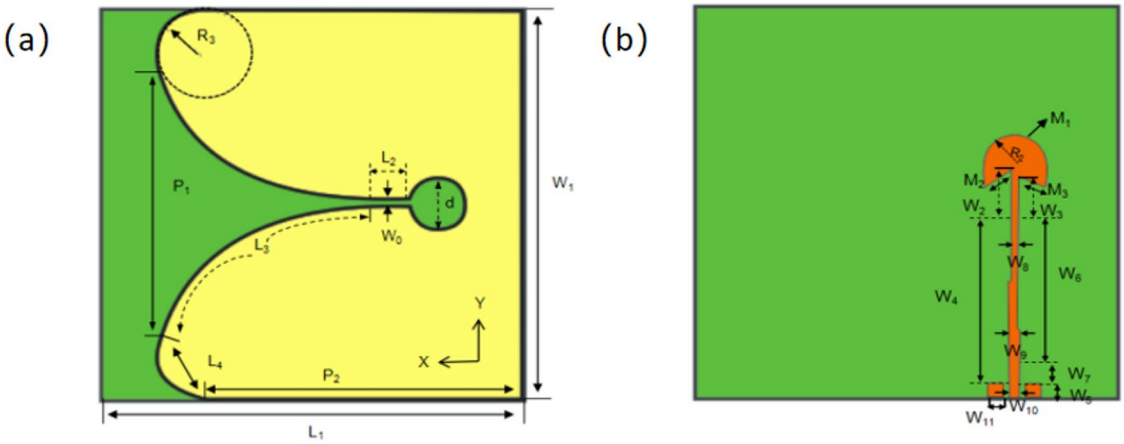

Fig. 10. The Vivaldi antenna structure: (**a**) front view; (**b**) back view.

Parameter	Size (mm)	Parameter	Size (mm)	Parameter	Size (mm)
L_1	80.0	W_4	31.4	W_8	1
W_1	80.0	W_5	2.5	W_9	2
H	1.0	W_6	25.4	W_{10}	2.5
L_2	3.25	W_7	5.0	W_{11}	3
L_3	55.0	M_1	26.2	R_2	6.25
L_4	19.7	M_2	5.8	R_3	10
W_0	2	M_3	5.4	P_1	52.22
W_2	8.1	W_3	7.36	P_2	59.32
d	10.5				

Table 1. Basic parameters of the Vivaldi antenna design.

antenna's electrical connectivity, ensuring transmission stability at higher frequencies, while the 0.5 mm via diameter effectively suppresses parasitic effects, providing an ideal balance of gain and directivity.

The final antenna structure is shown in Fig. 10. The antenna employs a microstrip feed to achieve good matching with a 50Ω coaxial cable, commonly used in practical applications. By adjusting the microstrip width (W_0 = 2 mm) and the dielectric constant (ε_r) of the substrate material, the characteristic impedance of the microstrip line is set to 50Ω, minimizing adverse effects on S-parameters and VSWR. The final optimized antenna structure features excellent impedance matching, and by controlling its geometry, the final dimensions are determined to be 80 mm × 80 mm × 1 mm.

The basic parameters of the antenna design are listed in Table 1.

Performance of the optimized Vivaldi antenna

This study conducted a comprehensive simulation analysis of the Vivaldi antenna featuring a 10 mm arc radius, nine vias, and a 0.5 mm via diameter using ANSYS simulation software. The simulation covers key performance metrics such as VSWR, S-parameters, gain, and electric field intensity distribution.

VSWR, S-parameters, and gain

As depicted in Fig. 11a, the optimized Vivaldi antenna exhibits a more stable VSWR across the 1.6–8 GHz frequency band, particularly in the critical 2–4 GHz range for medical imaging. The VSWR consistently remains below 1.5, indicating better impedance matching characteristics in this frequency range. This effectively reduces signal reflection losses and significantly enhances transmission efficiency. Compared to the traditional antenna, the optimized design improves transmission efficiency by minimizing signal reflection and transmission loss, thereby enhancing the signal-to-noise ratio. This makes the antenna particularly advantageous for medical imaging applications, where signal quality is crucial, offering higher imaging speed and signal stability.

Figure 11b illustrates that the optimized antenna has a lower reflection coefficient at several frequency points, especially around 4 GHz, where the S11 value drops to approximately − 45 dB, compared to around − 20 dB for the traditional antenna. This difference indicates superior return loss performance at key frequencies, reducing reflection losses and allowing the signal to be transmitted more effectively to the detection area. Additionally, the optimized antenna demonstrates a more stable S11 curve in the 2–8 GHz band, with smaller fluctuations in the reflection coefficient, enhancing multi-frequency transmission stability. These improvements increase the

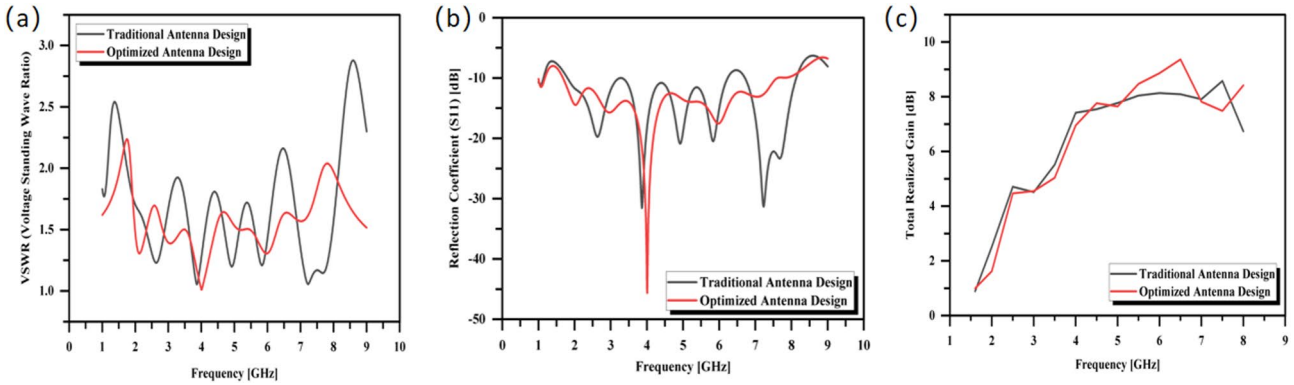

Fig. 11. Performance of the traditional and optimized Vivaldi antennas in the 1.6 GHz to 8 GHz frequency band: (**a**) VSWR; (**b**) reflection coefficient (S11); (**c**) Gain.

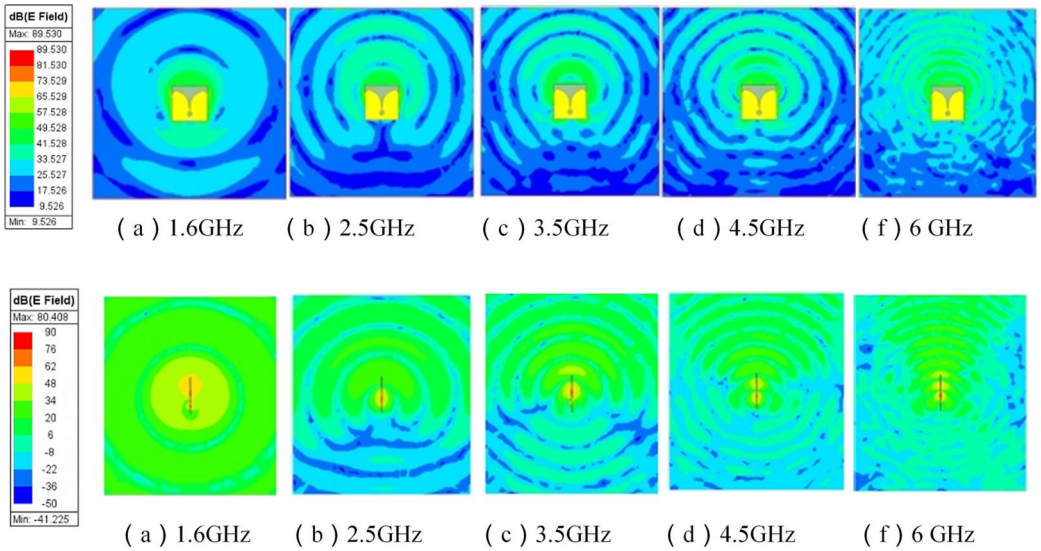

Fig. 12. Electric field distribution of the miniaturized coplanar Vivaldi antenna: The top image is the front view, and the bottom image is the top view.

signal's penetration ability and deep detection performance, thereby enhancing sensitivity and imaging clarity for brain hemorrhage detection.

From the gain curve in Fig. 11(c), it is evident that the optimized antenna displays a smoother gain curve in the 4–6 GHz frequency range, achieving a peak gain of about 9.5 dB, which is slightly higher than that of the traditional antenna. A higher and more stable gain means that the optimized antenna can provide a stronger signal when penetrating tissue, resulting in higher resolution images during imaging.

Electric field intensity distribution

The variation of the electric field intensity of the Vivaldi antenna at different frequencies is shown in Fig. 12, accompanied by both front and side views. The front view reveals that, at the low frequency of 1.6 GHz, the electric field intensity is concentrated at the center of the antenna, exhibiting high energy density but a limited radiation range, making it suitable for imaging shallow tissues. As the frequency increases, particularly at 2.5 GHz and 3.5 GHz, the high-intensity region expands, coverage increases, and the energy distribution becomes more uniform, enhancing the antenna's capability to detect deeper tissues. This enhancement improves the antenna's capacity to detect medium-depth hemorrhagic lesions and contributes to enhanced sensitivity and resolution in imaging. At higher frequencies, specifically at 4.5 GHz and 6 GHz, the electric field distribution is broad and uniform, with a significant spread of high-intensity regions, particularly evident at 6 GHz.

The side view indicates that as the frequency increases, the electric field intensity expands outward from the center of the antenna. In the low-frequency range, the radiation range is smaller, while at 2.5 GHz and 3.5 GHz, the energy distribution broadens and radiation efficiency improves. In the high-frequency range, especially at 6 GHz, the electric field intensity is most widely and evenly distributed, making it suitable for long-distance radiation and high-precision signal transmission.

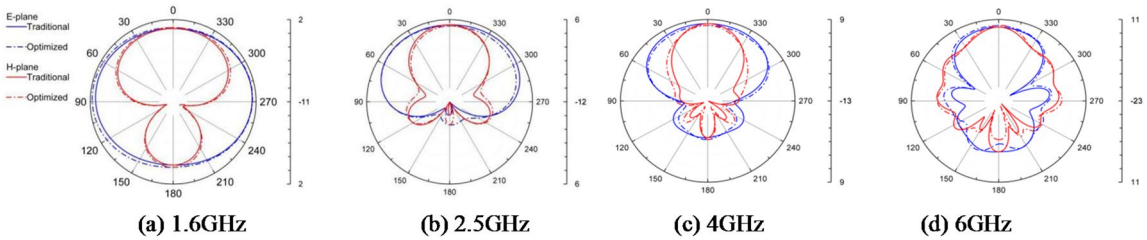

Fig. 13. 2D radiation patterns of the traditional and optimized Vivaldi antennas at 1.6 GHz, 2.5 GHz, 4 GHz, and 6 GHz.

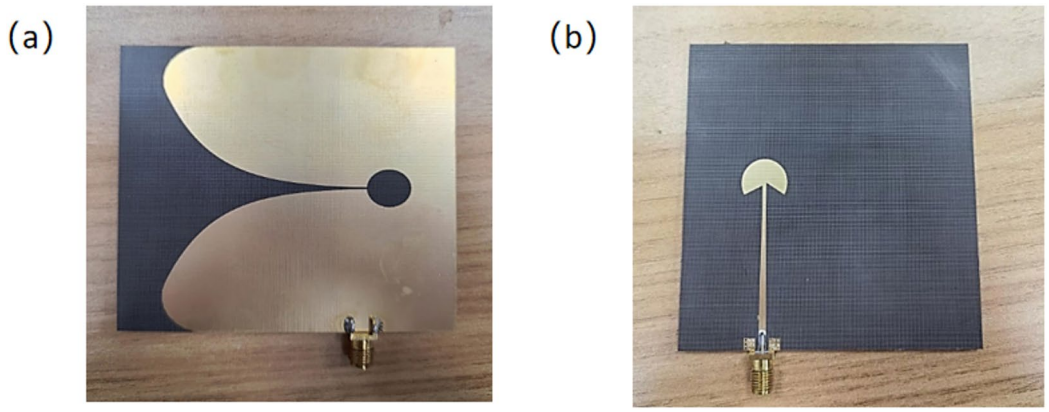

Fig. 14. Physical picture of the optimized Vivaldi antenna; (**a**) front; (**b**) back.

In summary, the electric field distribution characteristics of the Vivaldi antenna across different frequency bands strongly support its application in imaging at varying depths. The optimized radiation performance at medium to high frequencies excels in tissue penetration and signal transmission, providing a solid technological foundation for precise hemorrhage detection in medical imaging.

Radiation pattern

Figure 13 presents the 2D radiation patterns of the E-plane and H-plane for both the conventional antenna and the optimized Vivaldi antenna at four frequency bands: 1.6 GHz, 2.5 GHz, 4 GHz, and 6 GHz. The figure clearly illustrates the significant improvement in radiation directivity achieved through the optimized design, which is essential for enhancing the accuracy of hemorrhage detection.

As the frequency increases from 1.6 GHz to 6 GHz, the optimized antenna exhibits a marked increase in gain in the main lobe direction, with energy becoming more concentrated. This indicates excellent directivity and sidelobe suppression capabilities. At 1.6 GHz, both the optimized and conventional antennas show nearly omnidirectional radiation patterns, resulting in weaker directivity. By 2.5 GHz, the optimized antenna demonstrates a significant enhancement in main lobe directivity, improved sidelobe suppression, and increased signal transmission efficiency.

At the higher frequency bands of 4 GHz and 6 GHz, the optimized antenna exhibits higher energy concentration in the main lobe along with superior sidelobe suppression. This improvement in directivity and energy focusing is directly correlated with enhanced accuracy in hemorrhage detection. The optimized design significantly increases signal penetration depth and image contrast, thereby improving resolution and detection sensitivity for small and deep hemorrhagic lesions.

Performance of the optimized Vivaldi antenna

To verify the accuracy of the simulation results, a physical prototype of the optimized Vivaldi antenna was fabricated. PTFE was used as the substrate, and the antenna was manufactured using Printed Circuit Board (PCB) etching techniques. The physical fabrication of the pads and metallized vias is critical to the antenna's performance. The pads were precisely manufactured using laser cutting technology to ensure a good connection with the feed line, optimizing signal transmission and impedance matching. The vias were made using laser cutting and automated drilling techniques, and were metallized through copper plating to connect the multi-layer circuit, reducing resistance and inductance effects and optimizing signal transmission efficiency. This precise manufacturing process effectively enhanced the stability and performance of the antenna, providing stronger signal stability and imaging quality, especially in high-frequency and microwave imaging applications. After fabrication, the antenna was inspected for dimensional accuracy and welding quality to ensure it met design requirements. The physical prototype is shown in Fig. 14.

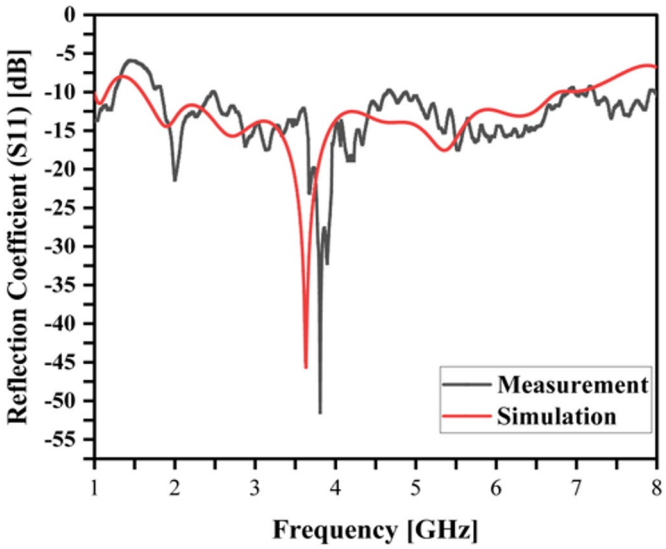

Fig. 15. Measurement diagram of the optimized Vivaldi antenna.

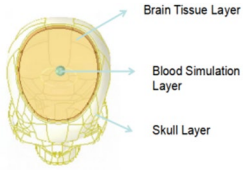

Fig. 16. Cranial model.

Tissue layer	Dielectric constant	Conductivity (S/m)
Skull layer	2.7	0.1
Gray/White matter layer	44	1.01
Blood layer	60	1.79

Table 2. Dielectric constant and conductivity parameters of cranial model (at 1.6 GHz)[32–34,37].

In the actual test, as shown in Fig. 15, the measured antenna showed good agreement with the simulation curve in the 1.6 GHz to 8 GHz frequency range, verifying the effectiveness of the antenna design.

Simulation analysis for brain hemorrhage detection using HFSS

Using ANSYS simulation software, this study employed an optimized Vivaldi antenna to simulate brain hemorrhage detection based on a three-layer cranial model.

Cranial model construction

To evaluate the feasibility of microwave detection for brain hemorrhage, this study utilized materials that closely match the electrical properties of actual brain tissues. The model consists of three layers, as shown in Fig. 16:

(1) Skull Layer: The dielectric properties of the skull were chosen to reflect laboratory-standard measurements, ensuring the model accurately represents the electromagnetic response of real tissues.

(2) Brain Tissue Layer: This layer simulates the combination of gray and white matter, providing a realistic representation of brain tissue characteristics.

(3) Blood Simulation Layer: This layer represents the hemorrhage area. A spherical blood capsule was used to simulate the electrical characteristics of the hemorrhage area, allowing for precise modeling of the interaction between microwave signals and the presence of blood.

This multi-layered approach enhances the accuracy of the simulation in assessing microwave detection capabilities for brain hemorrhage.

We conducted the simulation in ANSYS HFSS. The dielectric constant and conductivity parameters of each layer's material are presented in Table 2, based on data from the International Virtual Population Database (IT'IS Foundation)[32] and relevant literature[33,34,37].

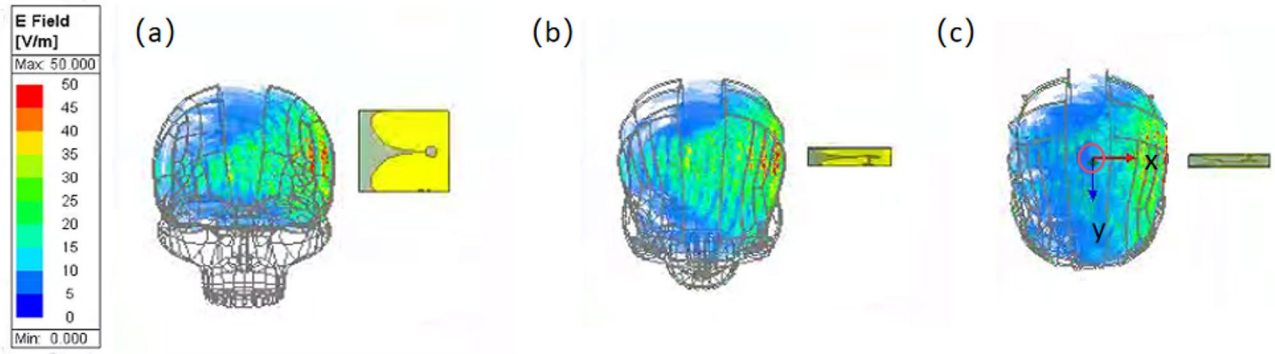

Fig. 17. Electric field distribution of a single antenna on the head at 2 GHz. (**a**) Normal head front view; (**b**) Normal head top view; (**c**) Bleeding head top view.

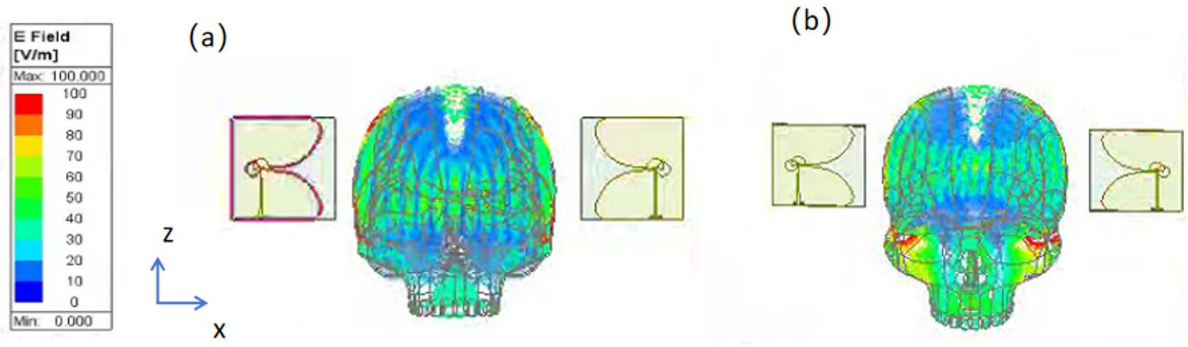

Fig. 18. Electric field distribution of dual antennas on the head at 2 GHz. (**a**) Front view of a normal head; (**b**) Front view of a hemorrhagic head.

Vivaldi antenna detection performance simulation

To evaluate the effectiveness of Vivaldi antennas in brain detection, this study simulated and analyzed the electromagnetic field distribution and signal penetration capabilities of the antenna across the frequency range of 1.6 GHz to 4 GHz. We focused on comparing the electric field distributions between normal brain tissue and hemorrhagic areas. Using both single-antenna and dual-antenna configurations, the study explored the performance of the antenna systems in detecting brain hemorrhages under different setups, providing a comprehensive assessment of their effectiveness.

In order to ensure simulation accuracy and efficiency, this study set the mesh size to 5 mm in HFSS, and applied radiation boundary conditions, setting them to 20 mm from the furthest edge of the antenna to avoid signal reflection and optimize computational resources, ensuring effective capture of the antenna performance.

1) Single Antenna Configuration.

First, we simulated a single-antenna configuration by positioning the antenna on one side of the skull model (Fig. 17). This setup allowed us to analyze the antenna's electromagnetic field distribution and signal penetration depth.7. The simulation results show that a single antenna generates a strong electromagnetic field suitable for shallow tissue detection. Within the 0–20 mm depth range, the electric field strength reaches up to 35 V/m, demonstrating excellent shallow detection performance. However, as the wave penetrates deeper into the skull, the field strength drops significantly—to 15 V/m at a depth of 40 mm. This represents a 57.14% decrease compared to the surface. When a hemorrhagic area is present at this depth, the field strength further drops to 5 V/m, indicating a 66.7% increase in attenuation compared to normal brain tissue. This attenuation is mainly caused by increased reflection, scattering, and absorption due to the dielectric contrast between blood and brain tissue.

2) Double-Antenna Configuration.

To further improve detection performance, this study introduced a dual-antenna face-to-face configuration, building on the single-antenna setup, as shown in Fig. 18. In a normal skull model, the electric field is strongest at the surface, indicating good penetration ability. However, at a depth of 40 mm, the field strength drops to 30 V/m—an attenuation of about 66.67%. In the hemorrhagic model, the field strength in the affected area is even lower, falling to 15 V/m. This represents an additional 50% attenuation compared to the normal brain tissue at the same depth. Such a significant reduction limits the electromagnetic wave's ability to penetrate,

resulting in further field weakening. As a result, both the signal's propagation depth and detection sensitivity are compromised. These findings suggest that strong attenuation within hemorrhagic regions hinders the effective identification of deeper lesions.

Comparison of 18 and 36 antenna arrays for cerebral hemorrhage simulation

To enhance the accuracy of cerebral hemorrhage detection, this study compared the performance of a 36-antenna array with an 18-antenna array. Both configurations utilize a circular array design with a radius of 10 cm. As illustrated in Fig. 19(b), in the 36-antenna array, each antenna sequentially acts as a transmitter, while the remaining 35 antennas function as receivers, capturing the backscattered signals reflected from the head model. This transmit-receive setup generates 1,260 scanning positions (36×35), with 201 data points collected at each position to create a comprehensive head scan data set. In contrast, the 18-antenna array, as shown in Fig. 19(a), operates similarly, with each antenna serving as a transmitter in turn and the remaining 17 antennas receiving the backscattered signals. This configuration results in 306 scanning positions (18×17), with 201 data points also sampled at each position to form a complete head scan data set. Consequently, the data collection volume of the 18-antenna array is only 24% of that of the 36-antenna array.

In the HFSS simulation software, the head model consists of three layers of media: the skull, brain tissue, and a blood layer. The blood is represented as a spherical area with a radius of 8 mm. To ensure simulation accuracy, adaptive meshing technology is employed, with a mesh size set to 7.5 mm. The simulation boundary condition is configured as a radiation boundary with a frequency of 2 GHz. The entire simulation process is conducted on a high-performance computer system equipped with 4 TB of 4400 MHz memory, an Intel Xeon Gold 6418 H processor, and four RTX A6000 graphics cards, ensuring sufficient performance for large-scale data processing and efficient computing.

To evaluate the performance of antenna arrays in detecting cerebral hemorrhage, this study utilized the Microwave Electromagnetic Reconstruction Imaging Toolkit (MERIT) imaging toolbox to process the backscattered signal data from 1,260 scanning positions[35]. To suppress noise, real-time differential technology and an adjustable beam imaging algorithm were implemented to achieve high-precision imaging. The real-time differential technology generates change data for comparison by analyzing the electromagnetic wave scattering signals under both normal and hemorrhagic conditions[36]. The DAS algorithm enhances signal response in high-contrast areas through delay compensation and post-summation, thereby improving the sensitivity of cerebral hemorrhage detection and effectively identifying the changing characteristics of the scattering signal during bleeding.

Figure 20 illustrates the impact of the brain hemorrhage area on the image energy state, showcasing the imaging effects of the 18-antenna array (Fig. 20a) and the 36-antenna array (Fig. 20b) in detecting brain hemorrhage. The red areas in the images indicate regions with higher signal intensity, typically corresponding to the brain hemorrhage area, which are easily identifiable. Comparatively, the image quality of the 36-antenna array is significantly superior to that of the 18-antenna array. In the imaging produced by the 18-antenna array, signal strength is primarily concentrated in the center of the image. Due to the limited number of antennas, the resolution and contrast are low, resulting in some small-scale hemorrhage areas not being clearly displayed and the presence of artifacts that affect image accuracy. In contrast, the 36-antenna array offers a higher signal acquisition density and stronger signal penetration, resulting in a more uniform and clearer image, particularly in areas farther from the center, allowing for a more accurate representation of the hemorrhage area.

To investigate the impact of varying amounts of bleeding on the image energy state, this study conducted a simulation comparing image energy distribution under different bleeding volumes, building on previous experiments. We utilized the same 36-antenna array configuration as before to simulate bleeding areas of different sizes (e.g., 5 mm and 12 mm) and employed the MERIT imaging toolbox[35] for data processing and analysis.

Figure 21 presents the simulated imaging results of 5 mm and 12 mm bleeding areas using 36 antenna arrays positioned at (0,0,0). In Fig. 21(a), the imaging of the 5 mm bleeding area shows a smaller red region, indicating

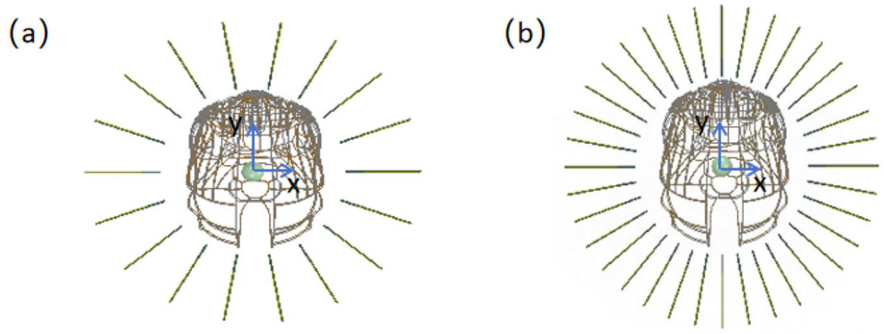

Fig. 19. Array-based simulation device for a hemorrhagic head featuring different antenna elements. (**a**) 18-antenna array; (**b**) 36-antenna array.

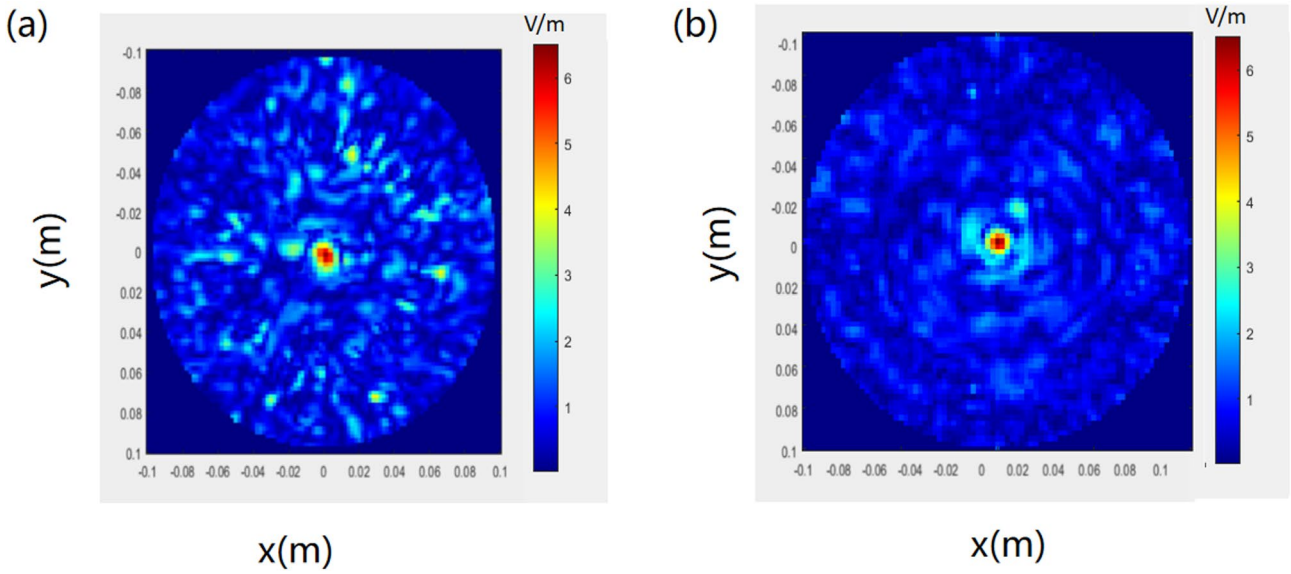

Fig. 20. Changes in image energy state due to the presence of brain hemorrhage[38–40]; (**a**) 18-antenna array; (**b**) 36-antenna array.

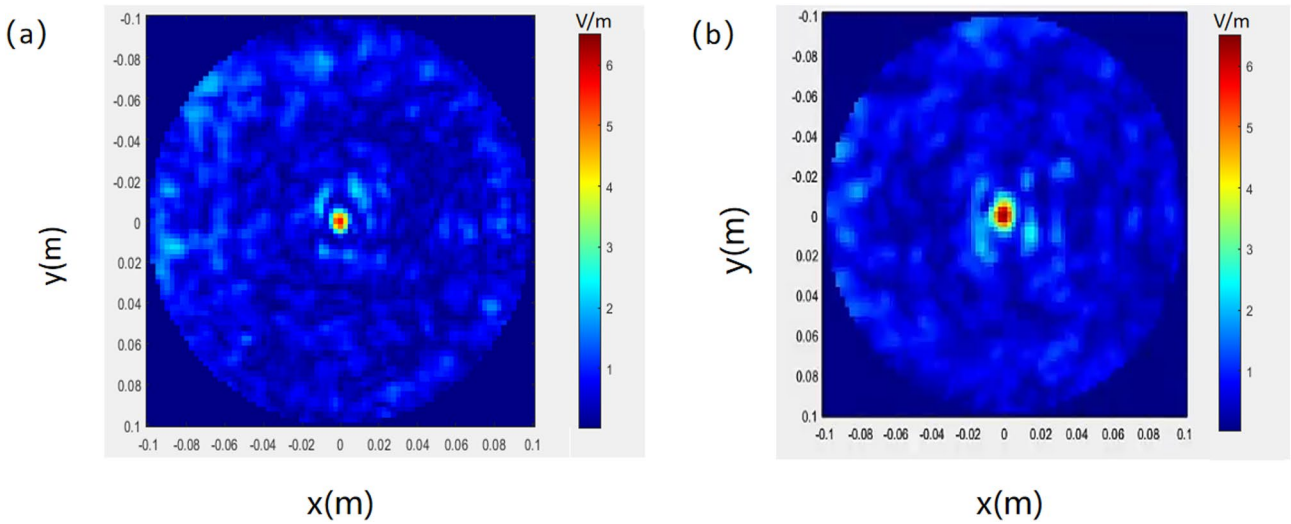

Fig. 21. Imaging results of bleeding using the 36-antenna array at the simulated position (0, 0, 0)[38–40]; (**a**) 5 mm; (**b**) 12 mm.

that the signal strength in this area is more concentrated. The signal variation is limited, with clear imaging details but minimal change. In Fig. 21(b), the imaging of the 12 mm bleeding area displays a significantly larger red area and a marked increase in signal strength, reflecting that a larger bleeding area causes more pronounced signal changes. Comparing the imaging effects of the two bleeding sizes demonstrates that the 36 antenna arrays can effectively detect signal strength variations resulting from different bleeding extents, with the signal change being proportional to the amount of bleeding.

System design and experimental validation of brain hemorrhage detection

Brain hemorrhage detection system setup

A UWB microwave imaging system for cerebral hemorrhage detection is proposed, as illustrated in Fig. 22. The system comprises two compact UWB Vivaldi antennas, a PXIe-8301 controller, a PXIe-1062Q chassis, and a Keysight M9370A two-port vector network analyzer (VNA), operating in the frequency range of 3 kHz to 4 GHz. Additionally, the device integrates a microcomputer, a display, and an antenna bracket. The VNA transmits the signal to the antenna via a coaxial cable, while the antenna emits the UWB microwave to the experimental model and receives the scattered signal for subsequent storage and processing.

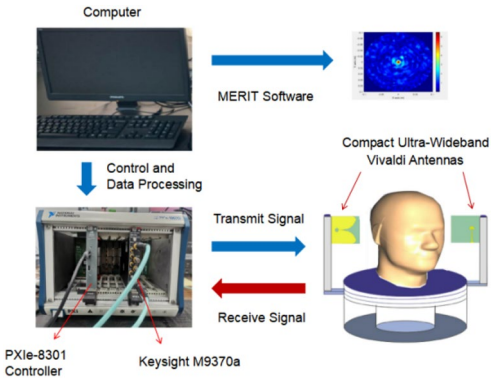

Fig. 22. Microwave imaging system.

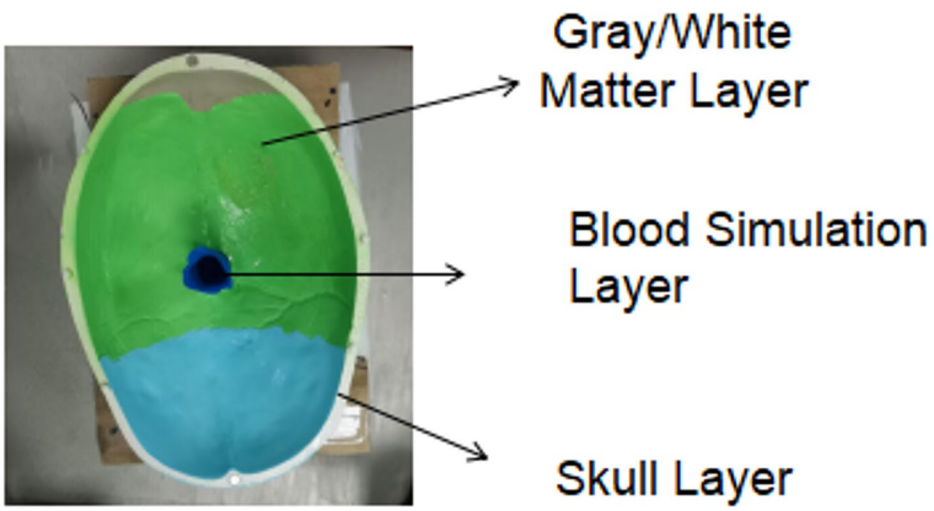

Fig. 23. Brain Hemorrhage Model.

Tissue layer	Glycerin (%)	Deionized water (%)
Gray/white matter layer	40	60
Blood layer	15	85

Table 3. Cranial model composition[37].

For data acquisition, 201 sampling points were utilized, extending the VNA's scan range to improve the capture of electromagnetic scattering characteristics within brain structures. The PXIe-8301 enabled rapid data transfer and control, connecting to an external computer via Thunderbolt 3. The system operates within the 1.6–4 GHz band, optimizing the balance between penetration depth and image resolution. The scattered signals are stored on a computer and analyzed to reconstruct the brain's electromagnetic field distribution.

Experimental microwave imaging system for cerebral hemorrhage detection

After constructing the brain hemorrhage detection system and optimizing the glycerol-water mixture as the coupling medium[37], we proceeded to experimentally simulate the brain hemorrhage region. A blue balloon was positioned at the center of the brain model, filled with a composition that mimicked blood, as illustrated in Fig. 23. This balloon was surrounded by layers representing brain tissue to accurately replicate the dielectric properties of gray and white matter.

Table 3 outlines the various ratios of glycerol-water solutions used to simulate the dielectric properties of brain tissue and the hemorrhage region, providing a more realistic experimental model for subsequent microwave imaging.

Building on this, we conducted microwave imaging experiments on the brain model using an antenna rotation configuration. The receiving end Vivaldi antenna rotated around the head model in 20° increments to achieve a total coverage of 340°. After each complete scan, the transmitting end Vivaldi antenna was synchronized to rotate 20° and move to the next position, continuing this process for a total of 18 positions to complete a full head scan. Data acquisition was conducted within the frequency range of 1.6 GHz to 4 GHz, collecting data at 201 frequency points in 0.012 GHz increments to ensure high accuracy in spectral resolution.

During signal acquisition, the computer is connected to the PXIe-8301 controller via a Thunderbolt 3 interface, enabling real-time control of the VNA for transmitting and receiving signals. The signals received by the antenna are transmitted to the VNA through coaxial cables, and the VNA then forwards the signals to the computer for storage and preliminary processing. To enhance imaging clarity and eliminate artifacts, the system employs real-time differential processing[36]. By overlaying the signal differences between the healthy head model and the hemorrhage model, this technique significantly amplifies the electromagnetic characteristics of the hemorrhage area, thereby minimizing the impact of interfering signals.

We processed the backscattered signals using the open-source MERIT software and applied the DAS and DMAS algorithms to reconstruct electromagnetic images of the brain model. The DAS algorithm quickly generated preliminary images of the lesion regions, as shown in Fig. 24(a). However, due to the influence of background noise, particularly scattering noise at the image edges, the signal-to-noise ratio (SNR) was low, and the edges of the hemorrhage area were blurred. For example, in the image, the signal strength in the hemorrhage area was approximately 6 V/m, while the background noise was 0.2 V/m, resulting in an SNR of approximately 30 dB for the DAS algorithm. Although the DAS algorithm is capable of quickly locating the hemorrhage area, its noise suppression ability is limited, leading to poor performance in high-precision imaging.

To further improve image quality, we employed the DMAS algorithm, which enhances the DAS algorithm by using delay, multiplication, and summation techniques to significantly enhance the signal and effectively suppress noise, as shown in Fig. 24(b). After applying the DMAS algorithm, the signal strength in the hemorrhage area increased to 6.5 V/m, while the background noise decreased to 0.1 V/m, resulting in an SNR of 65 dbs. By optimizing the SNR, the DMAS algorithm significantly improved the clarity of the signal, reduced background noise, enhanced the contrast and resolution of the hemorrhage area, and made the image edges clearer, further improving the imaging quality.

Experimental results demonstrate that the application of the UWB microwave imaging system in the simulated brain hemorrhage model validates its effectiveness and reliability in real tissue models and physical prototypes, showcasing its great potential for early brain hemorrhage diagnosis.

Experiments and results

Among the different types of antenna designs listed in Table 4, the mini coplanar Vivaldi antenna demonstrates outstanding performance in medical imaging, particularly in the detection of brain diseases such as brain hemorrhage imaging, due to its wide operating frequency range (1.6 ~ 8 GHz), low reflection loss (-45 dB), and high gain (9.5 dB). In comparison, the elliptical square patch antenna[8] (1.19 ~ 3.56 GHz) is suitable for low-frequency imaging but its lower gain (3.8 dB) and higher reflection loss (-40 dB) affect imaging quality. The microstrip patch antenna[9] (7 ~ 8 GHz) can be used for brain tumor detection, but its high frequency range limits penetration ability, which impacts imaging performance. The DGS-UWB monopole antenna[10]

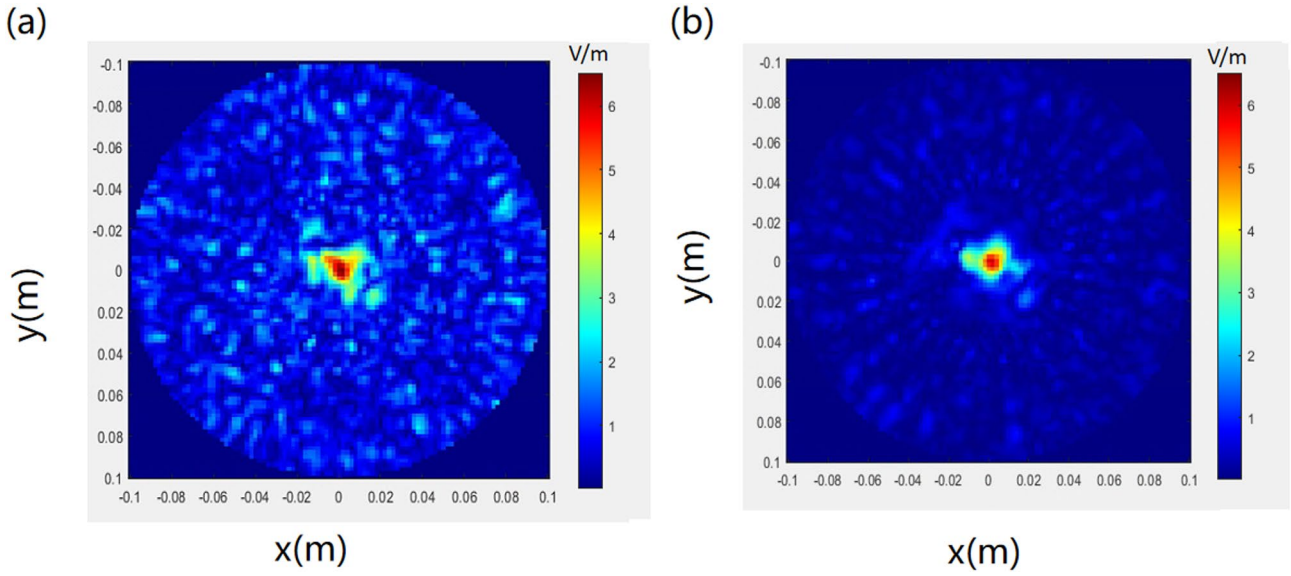

Fig. 24. Hemorrhage area imaging effects under different algorithms[39,40]; (**a**) DAS Algorithm Hemorrhage Imaging; (**b**) DMAS Algorithm Hemorrhage Imaging.

Literature	Antenna Type	Size (m^3)	Substrate	Bandwidth (GHz)	Max Gain (dB)	S11 Optimal Value (dB)	Algorithm	Application Effect
[8]	Elliptical Square Patch with Improved Slot Plan	70 × 60 × 1.5	FR4 (ε = 4.4)	1.19 ~ 3.56	3.8	-40	Not reported	Brain imaging, no imaging
[9]	Microstrip Patch Antenna	31.68 × 31.01 × 0.75	Not reported	7 ~ 8	Not reported	Not reported	Not reported	Brain tumor detection, too high frequency, parameter change detection
[10]	DGS-based UWB Monopole	50 × 50 × 1.5	RO3003 (ε = 3)	2.94 ~ 6.96	3.93	-32.59	Not reported	Penetrates brain tissue and tumors, but exceeds the 1–4 GHz range
[11]	New Side-Notched Vivaldi Antenna	45 × 35 × 0.79	Rogers RT / Droid 5870 (ε = 2.33)	3.9 ~ 9.15	4.65	-38	Not reported	Low image resolution, noise interference, hard to detect subtle lesions
[17]	Vivaldi Antenna with Radial Shorted Line, Resonant Cavity, and Conical Slot	50 × 50 × 1.5	Not reported	3.6 ~ 13.6	5.2	-39	Not reported	Microwave imaging, no imaging
[18]	Balanced Slot Reverse Vivaldi Antenna	40.1 × 40.1 × 1.6	Not reported	3.01 ~ 11	4.91	-31	DMAS	Detects tumors, but shape and size inconsistencies
[19]	Sierpinski Arrow Curve Vivaldi Antenna	65 × 65 × 1.6	RO4350B (ε = 3.66)	2.35 ~ 3.79	5.2	-35	Not reported	Penetrates three-quarters of the head model, but no imaging
[22]	M-CPVA Antenna	58.6 × 92 × 1.6	FR4 (ε = 4.4)	1 ~ 7.5	Not reported	-42 dB	Linear Sampling Method	Penetrates brain tissue, but low resolution, hard to detect small lesions
[24]	Sinusoidal Corrugated Antipodal Vivaldi Antenna	Not reported	Not reported	1.1 ~ 10	8.15	Not reported	it-DAS	Clearly detects breast cancer, but with location bias and artifacts
This paper	Miniaturized Coplanar Vivaldi Antenna	80 × 80 × 1	PTFE (ε = 2.65)	1.6 ~ 8	9.5	-45	DAS and DMAS	Can detect protruding tissue, clearly detects brain hemorrhage size changes

Table 4. Antenna performance comparison.

(2.94 ~ 6.96 GHz) can penetrate brain tissue and tumors, but its frequency range exceeds the ideal 1–4 GHz range, potentially causing signal attenuation and affecting image clarity. The new side-slot Vivaldi antenna[11] (3.9 ~ 9.15 GHz), though having high gain (4.65 dB), suffers from low imaging resolution due to noise interference and frequency range issues, making it difficult to detect subtle lesions. Furthermore, the Vivaldi antenna with radial short-circuit lines, resonant cavities, and conical slots[17]t> (3.6 ~ 13.6 GHz), as well as the sinusoidal groove reverse Vivaldi antenna[24] (1.1 ~ 10 GHz), although having higher gains (5.2 dB and 8.15 dB), are affected by noise interference in the high-frequency band, which destabilizes their imaging performance. The balanced-slot reverse Vivaldi antenna[18] (3.01 ~ 11 GHz), which utilizes the DMAS algorithm, is capable of detecting tumors, but its inconsistent shape and size lead to variable imaging results.

Overall, the mini coplanar Vivaldi antenna stands out in the precise imaging of brain diseases due to its wide frequency band, low reflection loss, and high gain, making it the preferred choice in medical imaging.

Conclusions

This study successfully designed and optimized a miniaturized coplanar Vivaldi antenna ($80 \times 80 \times 1$ mm^3) specifically for microwave imaging-based intracerebral hemorrhage (ICH) detection. The antenna incorporates innovative design features, including curved radiation arms, optimized pad layout, and precisely arranged metallized via holes, enabling exceptional signal penetration and imaging resolution across a wide frequency range from 1.6 GHz to 8 GHz. Experimental results demonstrate that within the critical medical imaging frequency range (2 GHz to 4 GHz), the antenna exhibits excellent impedance matching characteristics, with a minimum reflection coefficient reaching − 45 dB, ensuring efficient energy transmission and signal stability. Furthermore, its peak gain reaches 9.5 dB, which significantly improves signal penetration and tissue imaging quality compared to traditional designs. This performance provides a reliable technological foundation for ICH detection.

To thoroughly evaluate the imaging performance of the antenna, we analyzed the electric field intensity distribution, focusing on the attenuation characteristics in hemorrhagic regions. Additionally, we compared the performance of 36-element and 18-element antenna arrays in ICH detection to investigate the impact of antenna count on signal quality, imaging resolution, and sensitivity. Experimental results reveal that the 36-antenna array produces more uniform and clearer images thanks to its higher data acquisition density. It particularly excels at detecting small hemorrhages, thereby reducing the risk of misclassification. In contrast, while the 18-antenna array allows faster screening, its lower sampling density leads to lower image resolution. This limitation makes it more difficult to accurately detect small hemorrhagic regions and renders it more prone to imaging artifacts. The 36-antenna array, with its multi-angle data acquisition, effectively mitigates noise, improves signal consistency, and enhances hemorrhage region recognition. By contrast, the 18-antenna array is better suited for rapid screening and real-time monitoring.

Furthermore, we investigated the impact of different hemorrhage volumes on detection performance. Experimental results indicate that small hemorrhages (≈ 5 mm) can be detected, but with only minimal signal variation. In contrast, larger hemorrhages (≈ 12 mm) show significant signal enhancement and more pronounced electromagnetic changes. These findings suggest that as hemorrhage volume increases, it causes greater signal loss and variability in reflections. To further improve imaging accuracy, we conducted experiments on a realistic

head model. We integrated a rotating antenna mechanism (20° step size) and real-time differential imaging, along with beamforming algorithms in the MERIT software. The experimental results confirm that the proposed antenna significantly improves image clarity and contrast in hemorrhagic regions, thereby increasing the overall resolution of the microwave imaging system. Differential imaging effectively suppresses background noise, while beamforming optimizes signal focusing, thereby increasing hemorrhage detection sensitivity. Further validation demonstrates that the antenna can accurately capture the electromagnetic responses of hemorrhagic regions, providing stable imaging support for ICH detection and significantly improving overall diagnostic accuracy.

Despite the significant progress achieved in this study, several challenges remain. First, individual variations in brain tissue structure may affect imaging performance. Therefore, future research should expand the sample size, collect more diverse pathological data, and refine imaging algorithms to improve system adaptability and detection accuracy. Second, although the antenna has been successfully miniaturized, further reducing device size while maintaining high performance remains a key challenge. Future studies should explore the integration of advanced materials, innovative circuit designs, and optimized fabrication techniques to develop more compact and efficient antenna structures, thereby enhancing system portability and usability.

Future research will focus on several key areas. First, we will optimize signal processing algorithms to enhance anti-interference capabilities, making the system more suitable for dynamic environments such as emergency rooms and bedside monitoring. Second, we will improve the hardware design to increase portability and user-friendliness for real-time detection applications. Additionally, we will further integrate AI-based approaches, leveraging transfer learning and deep learning models to refine imaging quality. This will enable the system to dynamically adjust imaging parameters based on different tissue characteristics and pathological conditions, ensuring greater adaptability. Finally, we plan to conduct clinical trials to validate the system's effectiveness and reliability in real-world medical settings, while continuously optimizing imaging algorithms to further improve hemorrhage detection accuracy. The findings of this study establish a strong technical foundation for developing portable ICH detection systems and hold promise for applications in stroke screening, emergency medicine, and telemedicine. In summary, this work presents a technically robust and accurate approach for the early detection and diagnosis of intracerebral hemorrhage.

Data availability

The datasets used and analyzed during the current study are available from the corresponding author upon request.

Received: 14 December 2024; Accepted: 26 November 2025
Published online: 05 December 2025

References

1. Martin, S. S. et al. 2024 heart disease and stroke statistics: a report of US and global data from the American heart Association[J]. *Circulation* **149** (8), e347–e913 (2024).
2. Mobashsher, A. T. et al. Design and experimental evaluation of a non-invasive microwave head imaging system for intracranial haemorrhage detection[J]. *Plos One*. **11** (4), e0152351 (2016).
3. Lin, Y. et al. Emulation of brain metabolic activities based on a dynamically controllable optical phantom[J]. *Cyborg Bionic Syst.* **4**, 0047 (2023).
4. Zhan, X. et al. Differences between two maximal principal strain rate calculation schemes in traumatic brain analysis with in-vivo and in-silico datasets[J]. *J. Biomech.* **179**, 112456 (2025).
5. Fhager, A. et al. Microwave diagnostics ahead: saving time and the lives of trauma and stroke patients[J]. *IEEE. Microw. Mag.* **19** (3), 78–90 (2018).
6. Guo, L., Alqadami, A. S. M. & Abbosh, A. Stroke diagnosis using microwave techniques: review of systems and algorithms[J]. *IEEE J. Electromagnet. RF Microwaves Med. Biology*. **7** (2), 122–135 (2022).
7. Abbosh, A. et al. Clinical electromagnetic brain scanner[J]. *Sci. Rep.* **14** (1), 5760 (2024).
8. Talukder, M. S. et al. Compact ellipse shaped patch with ground slotted broadband monopole patch antenna for head imaging applications[J]. *Chin. J. Phys.* **72**, 310–326 (2021).
9. Sneka, C., Shuhaina, A. & Vidhya, B. *3rd International Conference on Electronics and Sustainable Communication* Systems *(ICESC)*. IEEE, 2022: 379–385. (2022).
10. Hossain, A. & Islam, M. A. *5th International Conference on Electrical Engineering and Information Communication* Technology *(ICEEICT)*. IEEE, 2021: 1–5. (2021).
11. Mahmud, M. Z. et al. Design and parametric investigation of directional antenna for microwave imaging application[J]. *IET Microwaves Antennas Propag.* **11**(6), 770–778. (2017).
12. Chareonsiri, Y., Thaiwirot, W. & Akkaraekthalin, P. Design of ultra-wideband tapered slot antenna by using binomial transformer with corrugation[J]. *Frequenz* **71** (5–6), 251–260 (2017).
13. Eichenberger, J., Yetisir, E. & Ghalichechian, N. Antipodal UWB Vivaldi antenna with pseudoelement and notched flares for 2.5–57 GHz applications[C]. In *2018 IEEE International Symposium on Antennas and Propagation & USNC/URSI National Radio Science Meeting*. IEEE, : 270–1758. (2018).
14. Amiri, M. et al. Exponential antipodal Vivaldi antenna with exponential dielectric lens[J]. *IEEE Antennas. Wirel. Propag. Lett.* **16**, 1792–1795 (2017).
15. Pandit, S., Mohan, A. & Ray, P. Metamaterial-inspired low-profile high-gain slot antenna[J]. *Microw. Opt. Technol. Lett.* **61** (9), 2068–2073 (2019).
16. Aktar, M. et al. Comparative analysis on antenna Balun and feeding techniques of step constant tapered slot antenna[J]. *J. Sens. Technol.* **10** (3), 31–45 (2020).
17. Sivasankari, S., Raja, P., Saranya, N. A. & Ultra-Wideband Vivaldi Antenna with Lozenge Shaped Slots for Biomedical Applications[C]. In *2023 International Conference on System, Computation, Automation and Networking (ICSCAN)*. IEEE, : 1–5. (2023).
18. Islam, M. T. et al. A homogeneous breast Phantom measurement system with an improved modified microwave imaging antenna sensor[J]. *Sensors* **18** (9), 2962 (2018).
19. Yazid, M. Y. et al. A Sierpinski arrowhead curve slot Vivaldi antenna for microwave head imaging system[J]. *IEEE Access.* **11**, 32335–32347 (2023).

20. Shi, Y. et al. An Ultra-wideband (UWB) High-gain Vivaldi Antenna for Detection of Cerebral Hemorrhage[C]. In *2022 International Conference on Microwave and Millimeter Wave Technology (ICMMT)*. IEEE, : 1–3. (2022).
21. Parveen, F. & Wahid, P. Detection of blood clots inside the brain using microwave Imaging[C] in *2022 3rd URSI Atlantic and Asia Pacific radio science meeting (AT-AP-RASC). IEEE*, : 1–4. (2022).
22. Uyanik, C., Demirel, S. & Akduman, İ. Miniaturized coplanar Vivaldi antenna design for brain imaging[J]. *Microw. Opt. Technol. Lett.* **65** (7), 2076–2083 (2023).
23. Paul, L. C. et al. Design and analysis of a UWB slotted Vivaldi antenna for microwave imaging applications. *IEIE Trans. Smart Process. Comput.* **12**(4), 350–357 (2023).
24. Asok, A. O., Tripathi, A. & Dey, S. Systematic performance evaluation for the detection of breast tumors with sinusoidal corrugated antipodal Vivaldi antennas utilizing DAS and It-DAS Methodologies[J]. *Progress Electromagnet. Res. C*, 137. (2023).
25. Palanisamy, S. et al. Miniaturized Stepped-Impedance resonator band pass filter using folded SIR for suppression of Harmonics[J]. *Math. Modelling Eng. Probl.*, **11**(8). (2024).
26. Sathishkumar, N. et al. Experimental investigations of dual functional substrate integrated waveguide antenna with enhanced directivity for 5G mobile communications[J]. *Heliyon*, **10**(17). (2024).
27. Palanisamy, S. et al. A novel approach of design and analysis of a hexagonal fractal antenna array (HFAA) for Next-Generation wireless communication. *Energies* **14**, 6204. https://doi.org/10.3390/en14196204 (2021).
28. Balanis, C. A. *Antenna Theory: Analysis and design[M]* (Wiley, 2015).
29. Pérez, M. et al. A UWB Vivaldi Antenna for TimeDomain Radar Applications[C] In *2022 IEEE International Symposium on Antennas and Propagation and USNCURSI Radio Science Meeting (APS/URSI)*. IEEE, : 19001901. (2022).
30. BALANIS, C. A. *Antenna Theory: Analysis and Design [M]* (Wiley, 2016).
31. Cabral, D. S. et al. Design of an antipodal Vivaldi antenna focusing on constructional Aspects[J]. *J. Microwaves Optoelectron. Electromagn. Appl.* **20**, 777–789 (2021).
32. https://itis.swiss/virtual-population/tissue-properties/database/dielectric-properties/.
33. Ireland, D. & Bialkowski, M. Microwave head imaging for stroke detection[J]. *Progress Electromagnet. Res. M.* **21**, 163–175 (2011).
34. Aldhaeebi, M. & Elshafiey, I. New antenna design for hyperthermia treatment of human head[C] In *2014 UKSim-AMSS 16th International Conference on Computer Modelling and Simulation*. IEEE, : 96–100. (2014).
35. O'Loughlin, D. et al. Open-source software for microwave radar-based image reconstruction[J]. (2018).
36. Puttock, J. et al. UWB microwave imaging for inclusions detection: Methodology for comparing artefact removal algorithms[C] In *Body Area Networks. Smart IoT and Big Data for Intelligent Health: 15th EAI International Conference, BODYNETS* Tallinn, Estonia, October 21, 2020, Proceedings 15. Springer International Publishing, 2020: 46–58. (2020).
37. Meaney, P. M. et al. Electrical characterization of glycerin: water mixtures: implications for use as a coupling medium in microwave tomography[J]. *IEEE Trans. Microwave Theory Tech.* **65** (5), 1471–1478 (2017).
38. ANSYS Inc. ANSYS HFSS 2023R1, ANSYS Electronics, 2023. [Online]. Available: https://www.ansys.com/en-in/products/electronics/ansys-hfss.
39. MathWorks, M. A. T. L. A. B. R. & Natick, M. A. 2022b, The MathWorks, Inc., USA, [Online]. (2022). Available: https://www.mathworks.com/products/new_products/release2022b.html.
40. EMFMed, M. E. R. I. T. I. Toolbox, GitHub Repository, 2024. [Online]. Available: https://github.com/EMFMed/MERIT.

Acknowledgements

I would like to thank Professor Zhengbin Li for his guidance and advice on technical issues.

Author contributions

Conceptualization: Weijia Zhang.Data curation: Jin Xie, Nutapong Somjit, Xinghua Liu.Formal analysis: Jin Xie, Xue Cheng.Investigation: Yanrong Jiang, Dongqin Sun.Resources: Nutapong Somjit, Shaomin Cai.Supervision: Weijia Zhang, Nutapong Somjit.Validation: Xue Cheng, Jin Xie.Writing – original draft: Jin Xie, Xue Cheng. Writing – review & editing: Weijia Zhang, Nutapong Somjit.

Declarations

Competing interests

The authors declare no competing interests.

Additional information

Correspondence and requests for materials should be addressed to S.C.

Reprints and permissions information is available at www.nature.com/reprints.

Publisher's note Springer Nature remains neutral with regard to jurisdictional claims in published maps and institutional affiliations.